Does thermotropic liquid crystalline self-assembly control biological activity in amphiphilic amino acids? – Tyrosine ILCs as a case study

Marco André Grunwald,[a] Selina Emilie Hagenlocher[¶,a] Larissa Turkanovic[¶,a] Soeren Magnus Bauch,[a] Sebastian Benedikt Wachsmann,[a] Luca Alexa Altevogt,[a] Max Ebert,[a] Julius Agamemnon Knöller,[a] Aileen Rebecca Raab,[a] Finn Schulz,[a] Mohamed A. Kolmangadi,[b] Anna Zens,[a] Patrick Huber,[c] Andreas Schönhals,[b] Ursula Bilitiewski*[d] and Sabine Laschat[ID]*[a]

Abstract. Amphiphilic amino acids represent promising scaffolds for biologically active soft matter. In order to understand the bulk self-assembly of amphiphilic amino acids into thermotropic liquid crystalline phases and their biological properties a series of tyrosine ionic liquid crystals (ILCs) was synthesized, which carried a benzoate unit with 0 – 3 alkoxy chains at the tyrosine unit and a cationic guanidinium head group. Investigation of the mesomorphic properties by polarizing optical microscopy (POM), differential scanning calorimetry (DSC) and X-ray diffraction (WAXS, SAXS) revealed smectic A bilayers (SmA_d) for ILCs with 4-alkoxy- and 3,4-dialkoxybenzoates, whereas ILCs with 3,4,5-trisalkoxybenzoates showed hexagonal columnar mesophases (Col_h), while different counterions had only a minor influence. Dielectric measurements revealed a slightly higher dipole moment of non-mesomorphic tyrosine-benzoates as compared to their mesomorphic counterparts. The absence of lipophilic side chains on the benzoate unit was important for the biological activity. Thus, non-mesomorphic tyrosine benzoates and crown ether benzoates devoid of additional side chains at the benzoate unit displayed the highest cytotoxicities (against L929 mouse fibroblast cell line) and antimicrobial activity (against *Escherichia coli* ΔTolC and *Staphylococcus aureus*) and promising selectivity ratio in favour of antimicrobial activity.

Keywords amino acids, cytotoxicity, ionic liquid crystals, self-assembly, antibiotic activity

---

[a] Institut für Organische Chemie, Universität Stuttgart, Pfaffenwaldring 55, D-70569 Stuttgart, Germany. E-mail: sabine.laschat@oc.uni-stuttgart.de

[b] Bundesanstalt für Materialforschung und –prüfung (BAM), D-12205 Berlin, Germany. E-mail: andreas.schoenhals@bam.de

[c] Institute for Materials and X-Ray Physics, Hamburg University of Technology, D-21073 Hamburg, Germany; Centre for X-ray and Nano Science CXNS, Deutsches Elektronen-Synchrotron DESY, D-22605 Hamburg; Centre for Hybrid Nanostructures ChyN, University Hamburg, D-21073 Hamburg, Germany, E-mail: patrick.huber@tuhh.de

[d] AG Compound Profiling and Screening, Helmholtz Zentrum für Infektionsforschung, Inhoffenstr. 7, D-38124 Braunschweig, Germany. E-mail: ursula.bilitewski@helmholtz-hzi.de

[¶] Contributed equally to this work

† Electronic supplementary information (ESI) available. See DOI:

Introduction

Ionic liquid crystals (ILCs) have received much attention over the last decade as battery materials,[1] novel electrolytes for organic solar cells,[2–4] anisotropic ion conductors,[5–7] electrofluorescent switches,[8,9] membranes for water desalination and waste water treatment[10] as well as other technical applications.[11] These unique soft matter materials can be tailored by variation of anion and cation leading to a broad range of polarities, viscosities, thermal and electrochemical stabilities as well as phase behaviour.[12–19] The bulk self-assembly of ILCs into various thermotropic mesophases is governed by strong Coulomb interactions between the ionic head groups and the corresponding counterions leading to nanophase separation of immiscible molecular subunits, i.e. ionic parts and non-polar, aromatic or fluorinated subunits. Mesophase formation and stability is further enforced by additional van der Waals, $\pi-\pi$ interactions, hydrogen bonding and/or fluorophobic interactions. On the one hand, the resulting lamellar, columnar or cubic mesophase architectures are indispensable for the various technical applications outlined above.[13] On the other hand, ILCs possess an amphiphilic molecular structure, suggesting that they may also interact with biological matter in a similar way as various known ionic liquids (ILs).[20–22] For example, Gravel and Schmitzer found that the electrostatic interactions of ILs (in their case imidazolium or benzimidazolium-based) with the cell membrane are one of the general requirements for affecting microorganisms. Furthermore, when alkyl chains were present, they could determine the self-association properties and the ability of the salts to insert into or diffuse through the cell membrane.[21] Eventually, early work by Douce revealed that ILCs can indeed shuttle oligonucleotides through cell membranes and that the chain lengths of the ILCs not only determined their phase type but also their ability to act as siRNA transfectants.[23] Later independent studies by Lin[24] and some of us[25] (Scheme 1) revealed antimicrobial properties of ILCs. In particular, amino acid-derived ILCs are promising candidates in that respect, as they resemble naturally occurring antimicrobial amino acid-containing lipids.[26–28] Because of their amphiphilic character and the relation to lipids which are essential building blocks in the lipid bilayer of bacterial cells, ILCs might be able to interact with and disrupt bacterial cell membranes. These properties would be highly desirable as they might contribute to the development of new antibiotics to counteract the increasing incidence of antibiotic resistance.[25,29–31] As a result, they may directly disrupt ion homeostasis or increase the penetration rate of concurrently administered antibiotics. Another interesting aspect would be what influence the respective mesophase geometry caused by self-assembly could have on the biological properties or specifically on the bacterial cell membrane. It is therefore important to further investigate and understand the potential of ILCs as antimicrobial agents. Several groups worldwide have investigated amino acid ILCs (and ILs) and the major focus was put on their thermotropic[25,32–37] and lyotropic phase behaviour[34,38–46] as well as solvation properties.[37,47–51] Biological properties of amino acid ILCs, on the other hand, remain almost unexplored.[24,25]

In our previous work[25] we have shown that cytotoxic and/or antimicrobial properties of amino acid ILCs can be controlled by the type of amino acid, i.e. phenylalanine (Phe), tyrosine (Tyr) or 3,4-dihydroxyphenylalanine (DOPA), carrying zero, one or two alkoxy side chains respectively[25] (Scheme 1). On the other hand the type of amino acid (and in some cases the counterion and/or an attached crown ether) also determined the mesomorphic properties.[25,32,52,53] We surmised that an amino acid such as tyrosine might be a suitable model system to study structure-property relationships. We aimed to control both mesomorphic and biological properties by (i) extension of the aromatic tyrosine core with a benzoate and eventually branching towards a wedge-shaped molecular architecture and (ii) variation of the substitution pattern of the lateral benzoate and (iii) variation of size and coordination properties of the counterion. The extension with different benzoate building blocks appeared to be most promising since these core units are known to promote mesophases in liquid crystals and (guanidinium) ILCs.[52–57] Moreover, the ester groups could offer the advantage of a potential biological target group with possibilities for applications as antibiotics.[58] Benzoates are synthetically easily accessible and provide properties beneficial for the formation of mesophases. These include additional π-π interactions of the aromatic moieties and dipole interactions of the ester units. In addition, an increase in the rigid moiety can be achieved while maintaining flexibility through the linking ester unit. Our results revealed that core extension via benzoates is indeed beneficial for the biological properties, while the mesomorphic self-assembly is determined by the substitution pattern of the lateral benzoate and the counterion. The details are disclosed below.

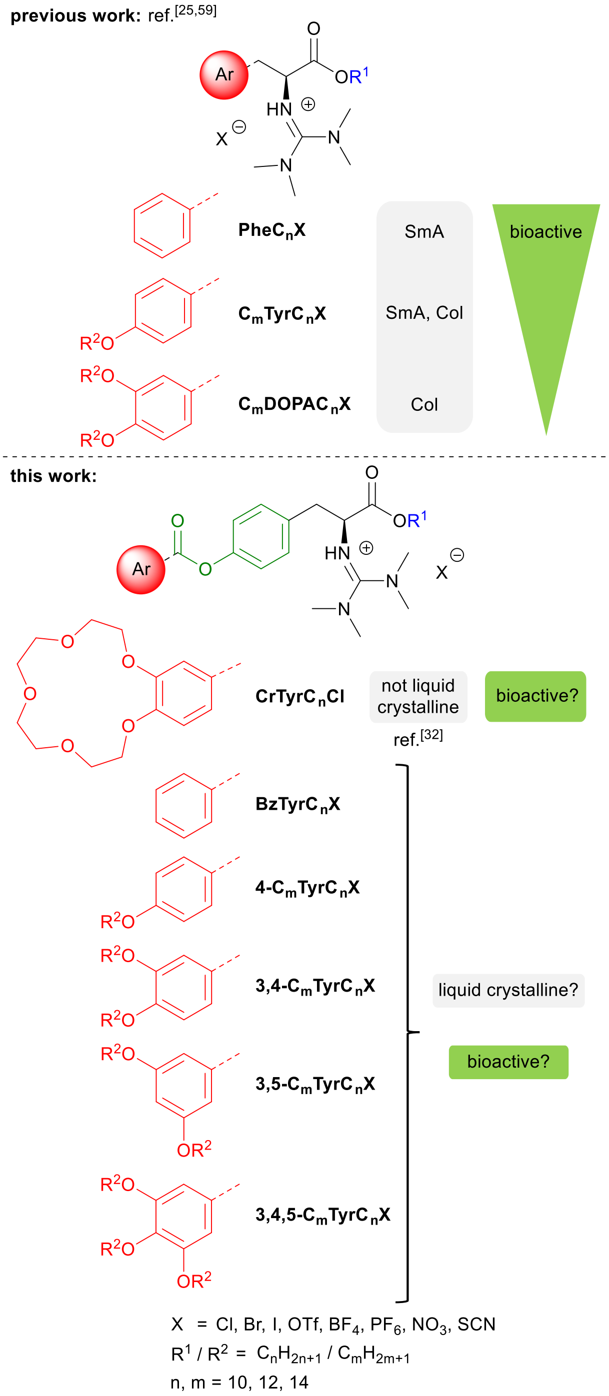

Scheme 1. Our previous work[25,32,59] on ionic liquid crystals derived from aromatic amino acids (top). Extension of the aromatic tyrosine core and its impact on both mesomorphic and biological properties (bottom).

Results and discussion

Synthesis of tyrosine-derived ILCs

As outlined in Scheme 2, L-tyrosine **Tyr** was treated with alkanols in the presence of 1.5 mol% TsOH under Dean-Stark conditions to give the esters **TyrC$_n$** in 66 – 93%.[32] Subsequent *N*-Boc protection with Boc$_2$O and NaHCO$_3$ yielded the NHBoc esters **TyrC$_n$Boc** in 88 – 96%, which were esterified with the alkoxybenzoates **Ar(C$_m$)CO$_2$H** in the presence of EDC and DMAP in CH$_2$Cl$_2$ following the method by Maloulibibout[32,60] to give the NHBoc benzoates **Ar(C$_m$)TyrC$_n$Boc** in 56 – 92%. Removal of the Boc group was accomplished with TFA according to Vallakati[61] yielding the corresponding amines **Ar(C$_m$)TyrC$_n$NH$_2$** in 63% – quant., which were reacted with tetramethylchloroformamidinium chloride **GuaCl** to the desired amphiphilic guanidinium chlorides **Ar(C$_m$)TyrC$_n$Cl** in 57 – 93%.

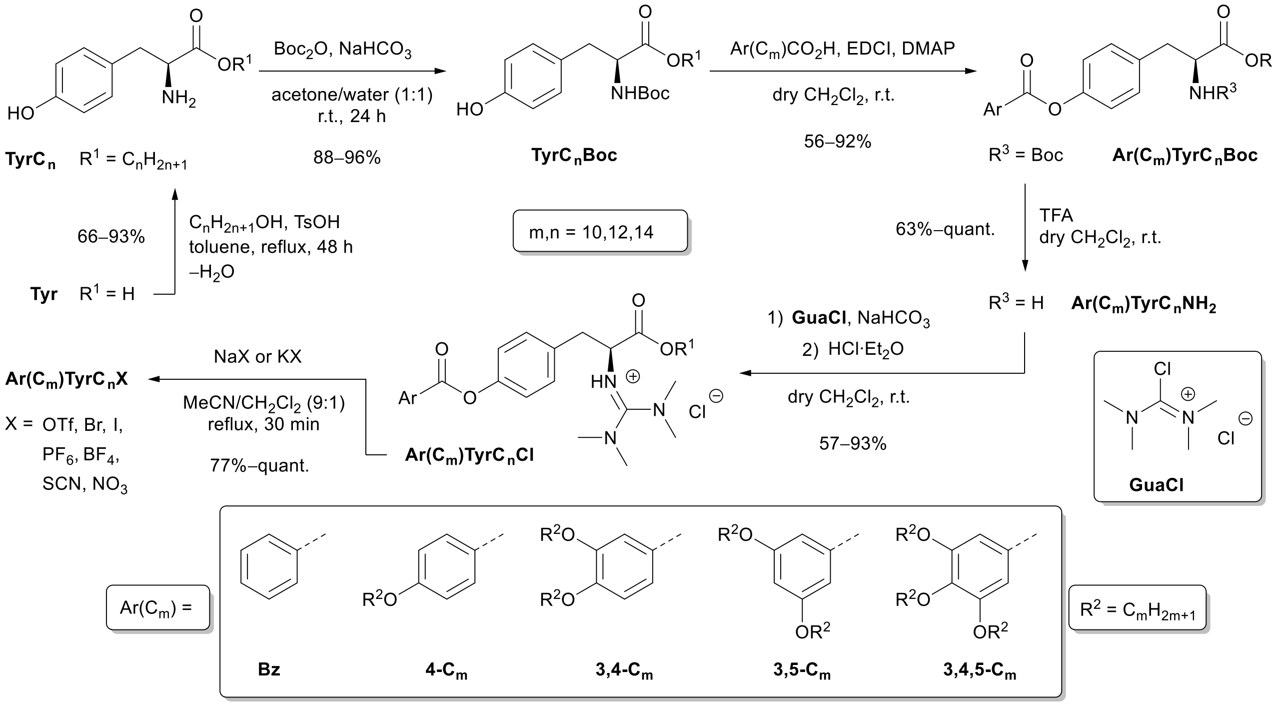

Scheme 2. Synthesis of tyrosine-derived guanidinium ILCs **Ar(C$_m$)TyrC$_n$X**.

The guanidinium chlorides **Ar(C$_{14}$)TyrC$_{14}$Cl** were then submitted to a salt metathesis with NaX or KX following the method by Butschies[62] to give the guanidinium salts **Ar(C$_{14}$)TyrC$_{14}$X** (X = Br, I, OTf, PF$_6$, BF$_4$, SCN, NO$_3$) in 77% – quant. yield. Attempts to synthesize analogous guanidinium chlorides by using L-serine instead of L-tyrosine met with little success and were discarded. For details see Scheme S2 and the corresponding part in the ESI (chapter 2.3).

NMR studies of tyrosine-derived ILCs

Examining the guanidinium salts **Ar(C$_m$)TyrC$_n$X** (Figure 1a, **3,4,5-C$_{14}$TyrC$_{14}$X** as example) via ^{1}H-NMR revealed a pronounced anion-dependent downfield shift of the guanidinium NH and the methylene H signals, presumably due to the tight ion pair of the counterion and the guanidinium head group (Figure 1b) in agreement with previous observations for guanidinium salts.[62–64]

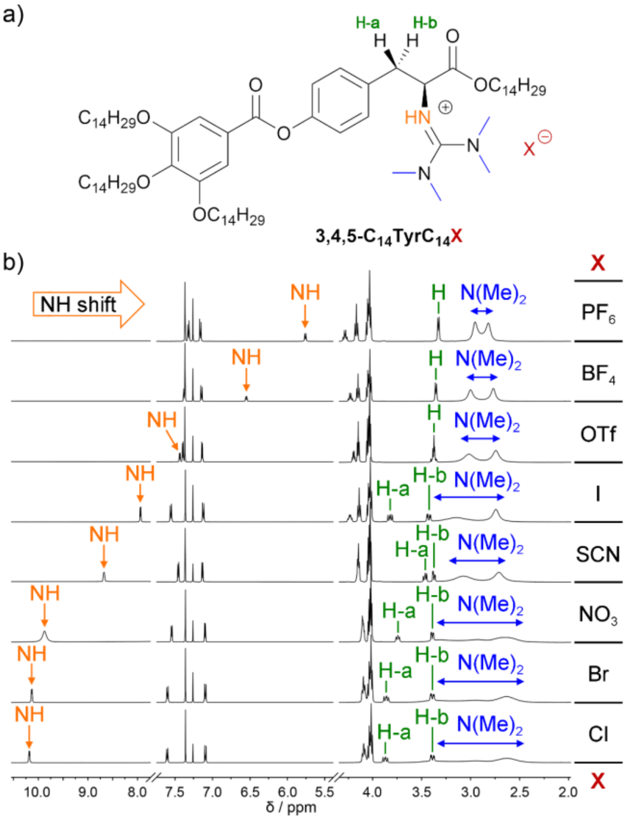

Figure 1. a) Structure and facilitated NMR assignment of **3,4,5-C$_{14}$TyrC$_{14}$X**. b) Sections of the ^{1}H NMR spectra of the guanidinium salts **3,4,5-C$_{14}$TyrC$_{14}$X** (500 MHz, $CDCl_3$, r.t.); orange arrow: shift δ_H of the NH signal (1H); blue double arrow: width of the guanidinium signals (total of 12H).

In addition, a concurrent influence on the position and splitting of the signals of the neighboring methylene group (3-H or 3a-H and 3b-H) and the methyl groups of the guanidinium head group [$N(CH_3)_2$] was observed.

Thus, a plot of the chemical shift of the NH signal δ_{NH} vs. anion radius[65,66] (Figure 2) showed that the δ_{NH} values decreased with increasing anion radius, since the NH proton experiences a greater shielding and thus an upfield shift because of larger or more sterically demanding anions. In addition, an electron-withdrawing environment can reduce the shielding of the proton by its electron shell (deshielding) and thus leads to a downfield shift.

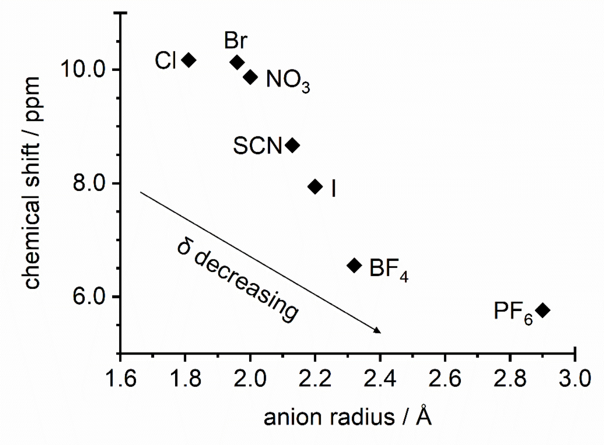

Figure 2. Correlation of the NH chemical shifts (in ppm, CDCl$_3$, 296 K) of **3,4,5-C$_{14}$TyrC$_{14}$X** (X ≠ OTf) with the anionic radii. The values for the radii were taken from lit.[65,66].

In order to study the dynamic behaviour of the guanidinium unit temperature-dependent ^{1}H NMR spectra were measured for selected guanidinium salts differing in their anions. The temperature during the NMR experiments was lowered stepwise from 298 K (r.t.) to 264 K (–9 °C). This resulted in splitting of the N(CH$_3$)$_2$ signals into four singlets of equal intensity (Figure 1c, light-blue arrows). The temperature-dependent NMR spectroscopic measurements of the guanidinium salts **3,4,5-C$_{14}$TyrC$_{14}$X** with the anions PF$_6$, BF$_4$ and SCN (Figure 3) revealed the influence of size of the anion. In the case of sterically more demanding anions, the protons generally have less space and therefore exhibit significantly more similar chemical shifts δH than in the case of simpler anions. The three relevant rotations within the guanidinium head group are shown in Figure 3 (far right). The rotations 1 – 3 refer to the rotation around the respective C–N bond axes. The temperature-dependent NMR spectroscopic measurements of the guanidinium salts **3,4,5-C$_{14}$TyrC$_{14}$X** with the anions PF$_6$, BF$_4$ and SCN were used to estimate the rotation barriers (Figure 3). The coalescence temperature T_{coa} describes the temperature at which several signals merge into one peak. The signal spacing $\delta\nu_{\text{coa}}$, which corresponds to the distance of the peaks at which coalescence occurs, was obtained directly from the ^{1}H NMR spectra rather than derived from a temperature-dependent plot because of the large difference between the temperatures. It should be noted that the determined free energies of activation $\Delta G^{\ddagger}_{coa}$ of the rotational barriers are estimated values which, according to Butschies,[62] nevertheless provide insight into the dynamics and behaviour of the guanidinium head group, due to a negligible temperature dependence of $\delta\nu_{coa}$. The position of the counterion with respect to the guanidinium group can be deduced from solid state structures.[62] However, no single crystal structures could be obtained for our derivatives and thus assignment of rotations was carried out in analogy with guanidinium salts described by Butschies.[62] Estimated rotational barriers of 55 – 58 kJ · mol^{-1} were obtained (Figure 3), which were of similar order of magnitude as previously described for guanidinium iodide (46 – 64 kJ · mol^{-1}).[62] The coalescence or splitting of the signals of the iodides occurred in a much broader temperature range (231 – 324 K), this could be attributed to the larger anions (PF_6, BF_4 and SCN) and the associated restriction of motion of the head group.

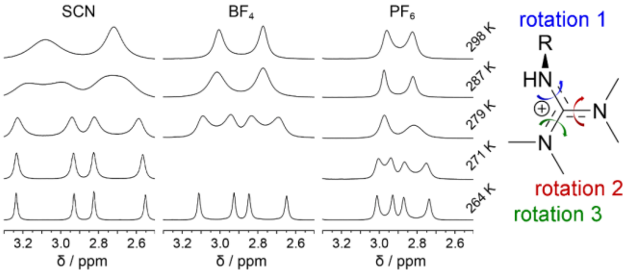

X	rotation	T_{coa} / K	$\Delta\nu_{coa}$ / Hz	k / Hz	$\Delta G^{\ddagger}_{coa}$ / kJ · mol^{-1}
SCN	3	298	254	564	57.3
	2	287	87	192	57.6
	2	279	144	319	54.8
	1	279	117	260	55.2
BF_4	3	287	122	270	56.7
	2	279	72	159	56.4
	1	279	71	158	56.4
PF_6	3	279	79	175	56.2
	2	271	33	73	56.6
	1	271	57	127	55.3

Figure 3. Sections of the temperature-dependent ^{1}H NMR spectra of guanidinium salts **3,4,5-C$_{14}$TyrC$_{14}$X** with X = SCN (left), BF_4 (center) and PF_6 (right) in the area of the guanidinium methyl groups (500 or 700 MHz, $CDCl_3$). Guanidinium methyl groups on the top right showing dynamic behaviour (for full temperature-dependent ^{1}H NMR spectra, see ESI chapter 10, Figure S28–S30). Rotations 1 – 3 were assigned according to the method by Butschies[62] and are summarized in the inserted table: coalescence temperatures T_{coa}, frequency seperations $\delta\nu_{coa}$, rate constants k and the estimated free energies of activation $\Delta G^{\ddagger}_{coa}$ of the guanidinium salts **3,4,5-C$_{14}$TyrC$_{14}$SCN**, **3,4,5-C$_{14}$TyrC$_{14}$BF$_4$** and **3,4,5-C$_{14}$TyrC$_{14}$PF$_6$**.

Mesomorphic properties of tyrosine-derived ILCs

Mesomorphic properties were studied by differential scanning calorimetry (DSC), polarizing optical microscopy (POM) and X-ray diffraction (XRD: SAXS, WAXS). For details of the DSC measurements (Figures S7–S14 and Table S1–S7), for further POM images (Figure S1–S6) and XRD results (Figure S15–S20) see ESI chapter 3 – 6 respectively.

Benzoate- and 3,5-dialkoxybenzoate-substituted guanidinium salts **BzTyrC$_n$X** and **3,5-C$_m$TyrC$_n$X** did not show liquid crystalline properties irrespective of the counterion X or the alkyl chain length (Figure 4). Only a melting from the crystalline to the isotropic phase was observed upon heating. Upon cooling samples either vitrified into a glassy solid in most cases or crystallized with a pronounce hysteresis due to supercooling. It should be noted that soft, polarizable anions,[67] e.g. Br, I, BF_4, PF_6 decreased the melting transitions considerably, in particular for the **3,5-C$_{14}$TyrC$_{14}$X** series (Figure 4).

On the other hand, chain length variations had only a little influence on the phase behaviour, as exemplified for the chloride salts **BzTyrC$_n$Cl** and **3,5-C$_m$TyrC$_n$Cl**. In addition, all unsubstituted and 3,5-substituted derivatives can be considered ionic liquids since their melting points are below 100 °C. The unsubstituted benzoates **BzTyrC$_n$X** represent an extended L-phenylalanine ILC **PheC$_n$Cl** from Neidhardt[25] which possessed SmA$_d$ phases with increasing chain length n ($n \neq 10$) (Table 1).[25] The absence of a mesophase for **BzTyrC$_n$X** might be attributed to the additional flexibility of the ester linkage between the building blocks and decreased influence of van der Waals interactions resulting in less efficient nanosegregation. Comparison of the non-mesomorphic 3,5-disubstituted guanidinium salts **3,5-C$_m$TyrC$_n$X** with the L-DOPA ILC **C$_m$DOPAC$_n$Cl** from Neidhardt,[25] which formed columnar (Col$_h$) mesophases (see Table 1)[25] suggests that *meta*-substituted side chains in **3,5-C$_m$TyrC$_n$X** do not support efficient space filling and thus prevent both the formation of a columnar as well as smectic phase.

Table 1. Phase transition temperatures *T* in °C of guanidinium salts **4-C$_m$TyrC$_n$X, BzTyrC$_n$X, 3,4-C$_m$TyrC$_n$X, 3,4,5-C$_m$TyrC$_n$X** in comparison to those of **C$_m$TyrC$_n$X, PheC$_n$X C$_m$DOPAC$_n$X** from Lit[25,59] Cr: Crystalline; G: glass-like; SmA$_d$: smectic A$_d$; Col$_h$: columnar hexagonal; Col$_r$: columnar rectangular; I: isotropic liquid; values from DSC 1st or 2nd cooling cycle with cooling/heating rates of 5 K · min^{-1} or 10 K · min^{-1}; ⁕ Observed in POM.

X$^-$	n	m			**4-C$_m$TyrC$_n$X**		
Cl	10	10	Cr	55	I	⁕	
Cl	12	12	Cr	35	SmA$_d$	80	I
Cl	14	14	Cr	54	SmA$_d$	109	I
NO$_3$	14	14	Cr	45	SmA$_d$	100	
I	14	14	Cr	44	SmA$_d$	101	I
BF$_4$	14	14	Cr	40	SmA$_d$	97	I
PF$_6$	14	14	Cr	30	SmA$_d$	84	I
X$^-$	n	m			**C$_m$TyrC$_n$X**		
Cl	10	10	G	30	SmA	79	I
Cl	12	12	G	27	SmA	112	I
Cl	14	10	Cr	36	SmA	87	I
Cl	14	12	Cr	36	SmA	106	I
Cl	14	14	Cr	45	SmA	111	I
Br	14	14	Cr	35	SmA	90	I
I	14	14	Cr	64	SmA	93	I
BF$_4$	14	14	Cr	31	SmA	87	I
PF$_6$	14	14	Cr	24	Col$_r$	78	I
OTf	14	14	Cr	19	SmA	32	I

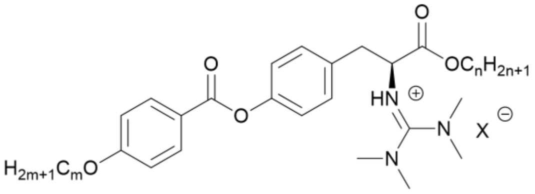

4-C$_m$TyrC$_n$X

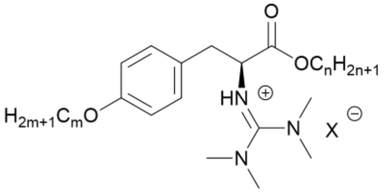

C$_m$TyrC$_n$X

X$^-$	n			**BzTyrC$_n$X**		
Cl	10	G	25	I		
Cl	12	G	37	I		
Cl	14	G	27	I		
Br	14	G$_1$	–36	G$_2$	15	I

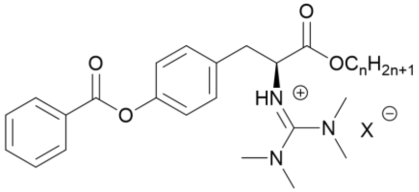

BzTyrC$_n$X

I	14	G	2	I		
PF_6	14	G_1	–45	G_2	6	I
BF_4	14	G	5	I		
NO_3	14	G_1	–46	G_2	21	I
X^-	n					**$PheC_nX$**
Cl	10	Cr	10	I		
Cl	12	Cr	26	SmA_d	57	I
Cl	14	G	20	SmA_d	52	I

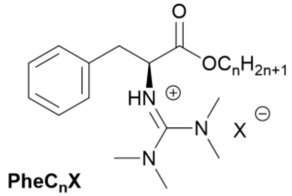

$PheC_nX$

X^-	n	m			**3,4-C_mTyrC_nX**					
Cl	10	10	Cr	27	SmA_d	85	I			
Cl	10	14	Cr_1	10	Cr_2	22	I	SmA_d	101	I
Cl	14	10	Cr	46	SmA_d	95	I			
Cl	14	14	Cr_1	10	Cr_2	31	I	SmA_d	95	I
X^-	n	m			**C_mDOPAC_nX**					
Cl	10	10	Cr	21	Col_h	46	I			
Cl	10	14	Cr	29	Col_h	46	I			
Cl	14	10	Cr	28	Col_h	54	I			
Cl	14	14	Cr	61	Col_h	134	I			
X^-	n	m			**3,5-C_mTyrC_nX**					
Cl	14	14	G_1	–13	G_2	35	I			
Br	14	14	G	–9	I					
I	14	14	G	–22	I					
PF_6	14	14	G	–12	I					
BF_4	14	14	G_1	–52	G_2	–12	I			
NO_3	14	14	G_1	–44	G_2	–1	G_3	33	I	

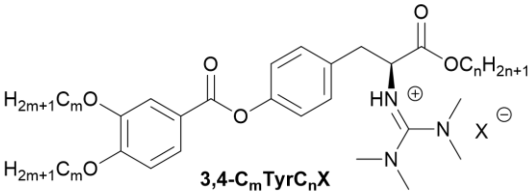

3,4-C_mTyrC_nX

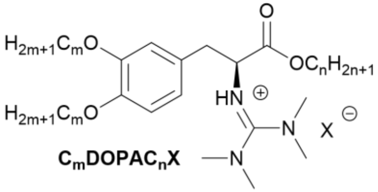

C_mDOPAC_nX

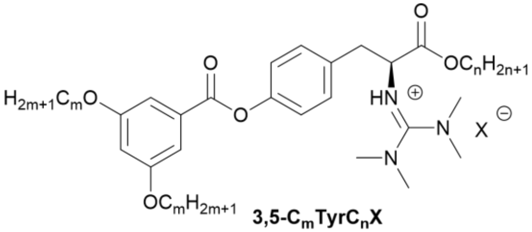

3,5-C_mTyrC_nX

X^-	n	m			**3,4,5-C_mTyrC_nX**					
Cl	10	10	Cr	47	I					
Cl	10	14	Cr_1	–4	Cr_2	45	I	Col_h	96	I
Cl	12	14	Cr_1	–11	Cr_2	14	I	Col_h	115	I
Cl	14	10	Cr	57	Col_h	105	I			
Cl	14	14	Cr	10	Col_h	92	I			

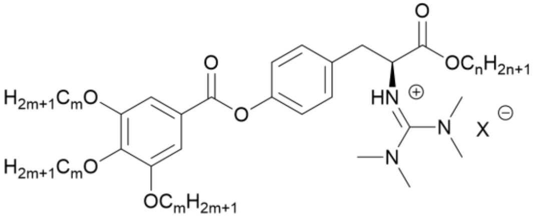

3,4,5-C_mTyrC_nX

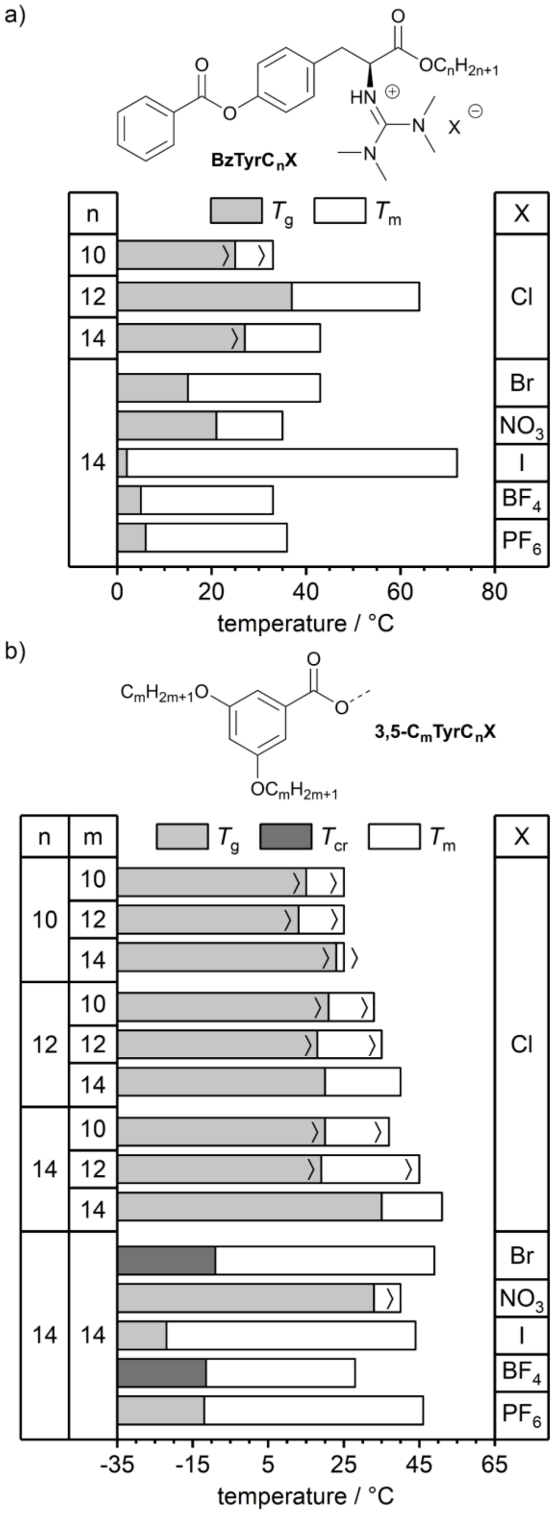

Figure 4. Results from DSC measurements (rounded values, 2nd heating, 2nd cooling, rate 5 K · min^{-1}) of **BzTyrC$_n$X** and **3,5-C$_m$TyrC$_n$X**. gray: solidification (T_g); dark gray: crystallisation (T_{cr}); white: melting point (T_m); 〉transition from POM; DSC data for **BzTyrC$_{14}$X**, **3,5-C$_{14}$TyrC$_{12}$Cl** and **3,5-C$_{14}$TyrC$_{14}$X** were obtained during 1st heating/cooling (decomposition).

In contrast, variation of the chain lengths for the 4-alkoxybenzoate chlorides **4-C$_m$TyrC$_n$Cl** revealed enantiotropic mesomorphism for all members (Figure 6, Table 1), except **4-C$_{10}$TyrC$_{10}$Cl**, which did not show any liquid crystalline behaviour and **4-C$_{12}$TyrC$_{10}$Cl** which exhibited a monotropic phase.

For the liquid crystalline members of the series **4-C$_m$TyrC$_n$Cl** the clearing transitions increase with increasing chain lengths m and n at both the ether and the ester moiety, while there was no such trend visible for the melting transitions. In general, longer side chains led to broader mesophases with the ester unit (C$_n$) having a more pronounced impact compared to the ether unit (C$_m$), e.g. ΔT for **4-C$_{14}$TyrC$_{10}$Cl** 16 K, **4-C$_{10}$TyrC$_{14}$Cl** 44 K, **4-C$_{14}$TyrC$_{14}$Cl** 55 K. Examination of guanidinium salts via POM showed fan-shaped textures, oily streaks, Maltese crosses and Bâtonnet textures with large areas of homeotropic alignment were visible, suggesting the presence of SmA phases (Figure 5a–c).

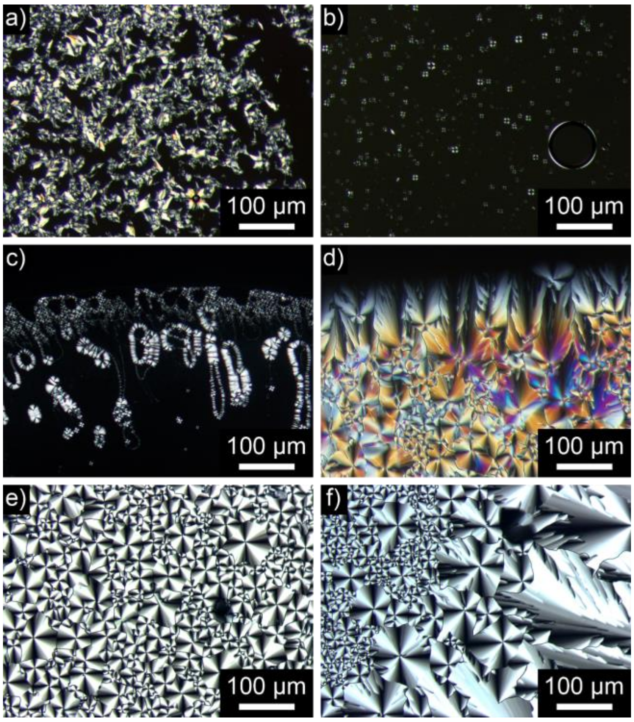

Figure 5. Exemplary POM images of selected guanidinium salts (100 × magnification): a) Bâtonnet of **4-C$_{14}$TyrC$_{14}$Cl** (101 °C), b) Maltese crosses of **3,4-C$_{12}$TyrC$_{12}$Cl** (93 °C), c) “oily streaks” of **3,4-C$_{14}$TyrC$_{14}$BF$_4$** (96 °C), d) fan-shaped textures of **3,4,5-C$_{14}$TyrC$_{12}$Cl** (106 °C), e) spherulitic textures of **3,4,5-C$_{14}$TyrC$_{14}$PF$_6$** (90 °C) and f) dendritic growth of **3,4,5-C$_{14}$TyrC$_{14}$I** (100 °C).

Anion exchange had a pronounced influence on the phase transition temperatures of **4-C$_{14}$TyrC$_{14}$X** (X = Cl, NO$_3$, I, BF$_4$, PF$_6$) (Figure 6, Table 1). With increasing size of the anion both melting and clearing points decreased while the mesophase widths remained around 55 K. The reduced phase transition temperatures are probably due to the decreased electrostatic interaction of the ionic sublayer within the SmA_d phase.

Comparison of the **4-C_mTyrC_nCl** with the parent tyrosine-derived ILC **C_mTyrC_nCl** (devoid of the benzoate unit) from Neidhardt[25,59] revealed no clear-cut trends of melting and clearing transitions (Table 1). On the other hand, similar trends were observed for both series **4-C_{14}TyrC_{14}X** and **C_{14}TyrC_{14}X**[25,59] upon anion exchange, i.e. both melting and clearing temperature decreased with increasing anion size. However, it should be noted that in the latter series the PF_6 counterion resulted in a change of the phase type to Col_r[59] as compared to the SmA phase for **4-C_{14}Tyr$C_{14}$$PF_6$**.

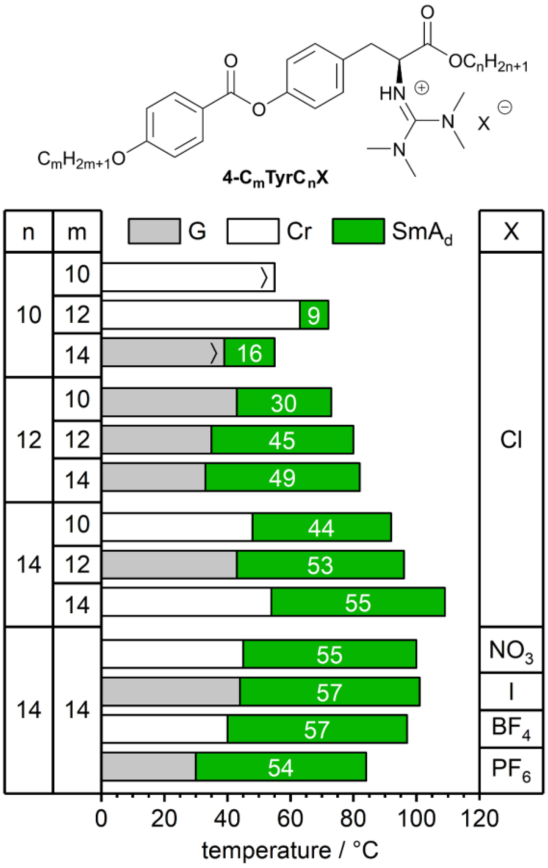

Figure 6. Mesophase widths from DSC measurements (rounded values, 2nd heating, 2nd cooling, rate 5 K · min^{-1}) of **4-C_mTyrC_nX**. gray: solidification (G); white: crystallisation (Cr); green: SmA_d; 〉transition from POM; DSC data for **4-C_{12}TyrC_{10}Cl**, **4-C_{12}TyrC_{14}Cl**, **4-C_{14}TyrC_{14}Cl** and **4-C_{14}TyrC_{14}I** were obtained during 1st cooling (decomposition); monotropic mesophase for **4-C_{14}TyrC_{14}I**.

Members of 3,4-dialkoxybenzoate chlorides **3,4-C$_m$TyrC$_n$Cl** displayed enantiotropic liquid crystalline properties except for compound **3,4-C$_{14}$TyrC$_{10}$Cl**, which was only monotropic (Figure 7). For the derivatives with C$_{10}$ ethers **3,4-C$_{10}$TyrC$_n$Cl** melting transitions remained relatively constant around ambient temperature while clearing transitions increased with increasing ester chain m, resulting in mesophase widths of 60 – 79 K. For ILCs with ether chains > C$_{10}$ both melting and clearing temperatures as well as phase widths remained relatively constant, the latter being in the range of 49 – 65 K. Under the POM large areas of homeotropic alignment were observed and Maltese crosses, oily streaks and Bâtonnet textures appeared mostly at phase boundaries, e.g. close to the coverslip indicating the presence of SmA phases.

Although the series **3,4-C$_n$TyrC$_m$Cl** resembles an extension of the known DOPA ILCs **C$_m$DOPAC$_n$Cl**,[25] their mesomorphism differed significantly (Table 1). While series **3,4-C$_n$TyrC$_m$Cl** showed SmA phases, the corresponding **C$_m$DOPAC$_n$Cl** derivatives showed columnar mesophases.[25] This different behaviour might be rationalized by different packing models, which will be discussed later.

In contrast to the **4-C$_{14}$TyrC$_{14}$X** series, anion exchange had only a small influence on the phase transition temperatures and temperature range of the mesophases of series **3,4-C$_{14}$TyrC$_{14}$X** (Figure 7)

Similar POM textures were observed as compared to the corresponding chloride salts suggesting that the phase type was not affected by the counterion (Figure 5a–c). In addition, most 4- and 3,4-substituted derivatives can also be considered as ionic liquids since their melting points are below 100 °C.

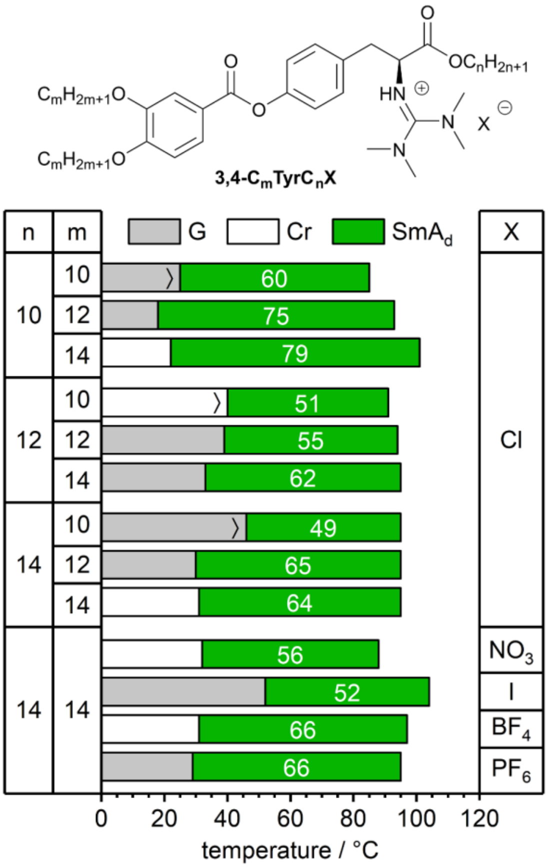

Figure 7. Mesophase widths from DSC measurements (rounded values, 2nd heating, 2nd cooling, rate 5 K · min^{-1}) of **3,4-C_mTyrC_nX**. gray: solidification (G); white: crystallisation (Cr); green: SmA_d; ⟩ transition from POM; DSC data for **3,4-$C_{10}TyrC_nCl$** were obtained during 1st cooling (decomposition); monotropic mesophases for **3,4-$C_{10}TyrC_{14}Cl$** and **3,4-$C_{14}TyrC_{14}I$**.

In the series of 3,4,5-trisalkoxy gallic ester chloride **3,4,5-C_mTyrC_nCl** several members **3,4,5-$C_mTyrC_{10}Cl$** (m = 10, 12), **3,4,5-$C_{10}TyrC_{12}Cl$** and **3,4,5-$C_{12}TyrC_{14}Cl$** were non-mesomorphic, while the other derivatives showed enantiotropic mesomorphism. In the DSC melting and/or clearing transitions were sometimes hardly visible and could only be identified by POM (Figure 8). Broad phase ranges were found mostly for those derivatives with C_{14} ether units, the most stable mesophase was observed for **3,4,5-$C_{14}TyrC_{12}Cl$** with a temperature range of 101 K. Under the POM fan-shaped and spherulitic textures with dendritic growth were observed (Figure 5c–e), suggesting the presence of columnar mesophases.

Anion exchange retained columnar mesophases for **3,4,5-$C_{14}TyrC_{14}X$** in most cases, except for **3,4,5-$C_{14}TyrC_{14}OTf$**, which was non-mesomorphic. For the thiocyanate salt the temperature range decreased considerably to 32 K, while all other derivatives with counterions X = Br, I, PF_6, BF_4, NO_3

displayed broad columnar phases of 72 – 89 K temperature range similar to the chloride salt. Additionally, most 3,4,5-substituted derivatives can be considered ionic liquids since their melting points are below 100 °C. POM textures of the members with different anions were similar to the textures of the corresponding chloride salt (Figure 5c–e). The occurrence of columnar hexagonal phases in the series **3,4,5-C$_m$TyrC$_n$X** was analogous to the DOPA derivatives **C$_m$DOPAC$_n$Cl** reported by Neidhardt, presumably due to the wedge-shaped molecular structure (Table 1).[25] Comparison of the two series revealed a certain bidirectionality for **3,4,5-C$_m$TyrC$_n$Cl**, i.e. clearing points as well as mesophase widths increased up to a certain chain lengths (n = 12, m = 14) and then decreased upon further increase of the chain lengths, whereas phase transitions and phase widths remained relatively constant for **C$_m$DOPAC$_n$Cl** until m = n = 14, where a significant increase was detected. The bidirectionality in the **3,4,5-C$_m$TyrC$_n$Cl** series suggests that the chain lengths n = 12, m = 14 provides optimum space filling and van der Waals interaction within this series, resulting in the broadest and most stable mesophase as compared to other chain lengths combinations.

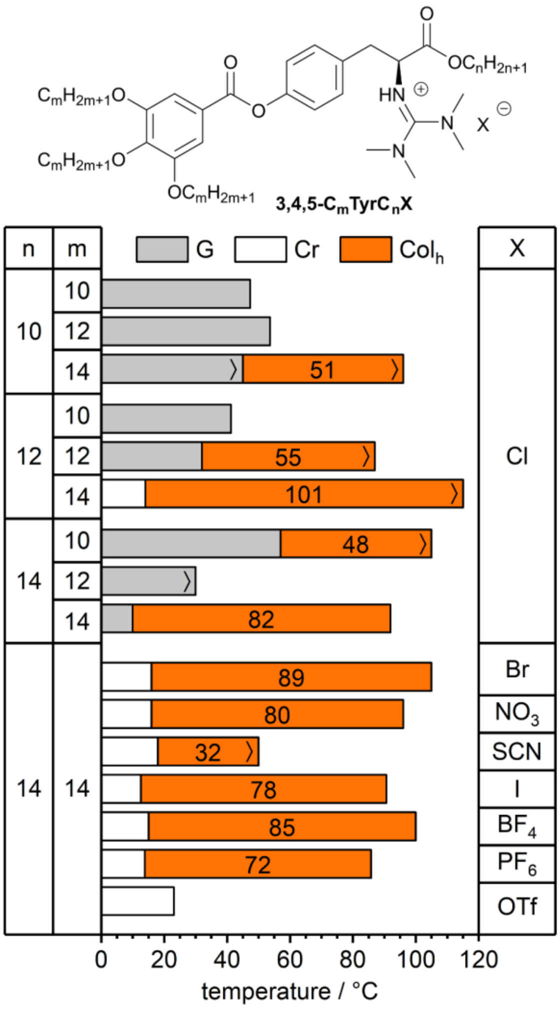

Figure 8. Mesophase widths from DSC measurements (rounded values, 2nd heating, 2nd cooling, rate 5 K · min^{-1}) of **3,4,5-C_mTyrC_nX**. gray: solidification (G); white: crystallisation (Cr); orange: Col$_h$; 〉transition from POM; DSC data for **3,4,5-C_{14}TyrC_{14}Br** were obtained during 1st cooling (decomposition).

In order to assign the phase geometries XRD studies of selected ILCs were performed. First, the calamitic 4-alkoxybenzoate chloride **4-C_{12}TyrC_{12}Cl** was examined. A sharp reflection at 2.5 ° in the small angle section and a broad diffuse reflex (halo) around 19.8 ° in the wide angle region were observed (Figure 9). The sharp reflex was assigned to the 1st order layer reflection (001) of the lamellar phase, while the halo was caused by the fluid-like alkyl chains. Unfortunately, no oriented samples could be obtained for the WAXS, SAXS measurements. For ILCs **4-C_{10}TyrC_{14}Cl** and **4-C_{14}TyrC_{14}Cl** similar WAXS and SAXS diffractograms were obtained (Figure S15a and b).

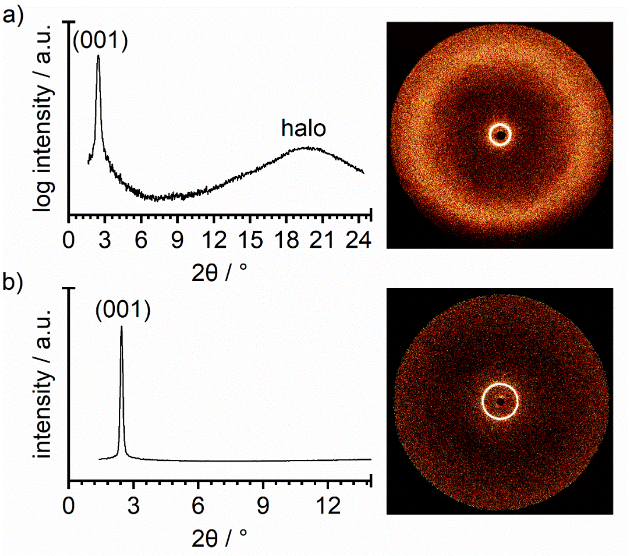

Figure 9. X-ray diffractograms (left) and 2D diffraction patterns (right) of **4-C_{12}TyrC_{12}Cl** at 74 °C in a) WAXS and b) SAXS.

From the distinct (001) reflection the layer distances d_{001} were calculated by using the Bragg equation. The results are summarized in Table . The d_{001} values increased with increasing ester chain lengths m from 35.1 Å (n = 10) via 36.1 Å (n = 12) to 37.8 Å (n = 14), whereas the halo d_{halo} remained relatively constant around 4.49 – 4.60 Å.

Table 2. X-ray diffraction data of the guanidinium chlorides **4-C_nTyrC_mCl** (SAXS). The measurements were performed during cooling from the isotropic liquid phase. The halo was determined from WAXS.

n	m	mesophase	T / °C	d spacing / Å	Miller indices
10	14	SmA_d	45	35.1	(001)
				4.50	halo
12	12	SmA_d	74	36.1	(001)
				4.49	halo
14	14	SmA_d	98	37.8	(001)
				4.60	halo

Temperature-dependent SAXS experiments of **4-C_{10}TyrC_{14}Cl** and **4-C_{12}TyrC_{12}Cl** revealed a decreasing layer distance d_{001} with increasing temperature, which is characteristic for a SmA phase (Figure 10). The layer shrinkage is caused by increased molecular mobility.[63,68–71] Due to thermal decomposition upon prolonged heating compound **4-C_{14}TyrC_{14}Cl** could not be examined in these experiments.

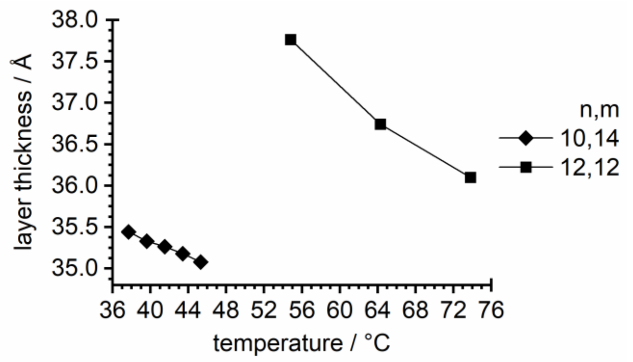

Figure 10. Determined layer distances d_{001} of **4-C$_{14}$TyrC$_{10}$Cl** and **4-C$_{12}$TyrC$_{12}$Cl** as a function of temperature.

Unfortunately, because of the nature of the compounds, single crystal structure analyses could not be performed for any of the guanidinium salt series **4-C$_m$TyrC$_n$Cl**, **3,4-C$_m$TyrC$_n$Cl** or **3,4,5-C$_m$TyrC$_n$Cl** to gain insight into the packing of the respective geometry. In order to still rationalize the observed lattice parameters, various modelling approaches were investigated, and different models were considered. For more details, please see chapter 7 in the ESI. However, if the obtained layer distances are compared with, for example, the calculated length L_{mol} = 50.5 Å of ILC **4-C$_{14}$TyrC$_{14}$Cl** in the extended *all-trans* conformation (Figure 11), it becomes apparent that partially interdigitated bilayers (SmA$_d$) rather than smectic monolayers (SmA$_1$) must be the case. The former are thereby also typically observed for ILCs.[13,72]

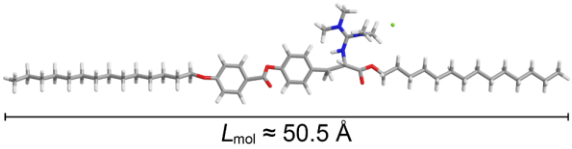

Figure 11. Structure of guanidinium chloride **4-C$_{14}$TyrC$_{14}$Cl** in extended form. C (gray); H (white); O (red); N (blue); Cl (light green).

Non-oriented samples of tyrosine-3,4-dialkoxybenzoates **3,4-C$_{10}$TyrC$_{14}$Cl**, **3,4-C$_{12}$TyrC$_{12}$Cl** and **3,4-C$_{14}$TyrC$_{14}$Cl** also revealed a sharp (001) reflection in the small angle section and a broad halo around 4.42 – 4.52 Å (Table 3, Figure 12, Figure S15c and d).

Table 3. X-ray diffraction data of the guanidinium chlorides **3,4-C$_n$TyrC$_m$Cl** (SAXS). The measurements were performed during cooling from the isotropic liquid phase. The halo was determined from WAXS.

n	m	mesophase	*T* / °C	*d* spacing / Å	Miller indices

10	14	SmA$_d$	74	39.7	(001)
				4.51	halo
12	12	SmA$_d$	68	37.8	(001)
				4.42	halo
14	14	SmA$_d$	74	39.7	(001)
				4.52	halo

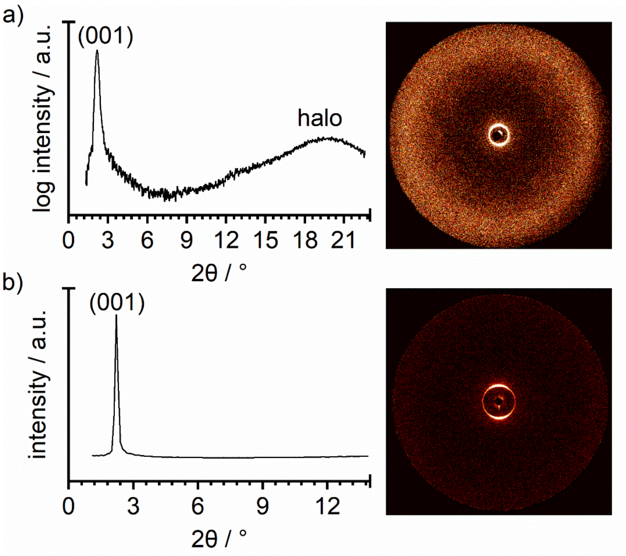

Figure 12. X-ray diffractograms (left) and 2D diffraction patterns (right) of **3,4-C$_{14}$TyrC$_{10}$Cl** at 74 °C in a) WAXS and b) SAXS.

In temperature dependent XRD experiments the d_{001} reflection decreased with increasing temperature confirming the SmA phase (Figure 13). The appearance of a SmA phase instead of a columnar phase (which was observed for **C$_m$DOPAC$_n$Cl**)[25] can be attributed to the extension of the system by one phenyl unit. This counteracts the side chain expansion (pizza slice-shaped favors Col) and favors a more rod-like shape and therefore an SmA phase.[73] The results in Table showed that the ether chains (chain length m) have a much larger impact on the layer spacing as compared to the ester chain. For example, both ILCs **3,4-C$_{10}$TyrC$_{14}$Cl** and **3,4-C$_{14}$TyrC$_{14}$Cl** possessed the same layer spacing d_{001}. Apart from this, the 3,4-substituted chlorides should have an analogous packing model to its 4-substituted derivatives, which is also discussed in more detail in chapter 7 in the ESI. Eventually, the wider layers compared to derivatives **4-C$_m$TyrC$_n$X** can be attributed to the additional chain (2 vs. 1). The derivatives **4-C$_m$TyrC$_n$X** have only one alkoxy chain attached to the benzoic acid building block, so they have to fill a larger amount of free space with a smaller number of chains. This can result in a shrinkage of the layer compared to **3,4-C$_m$TyrC$_n$X**.

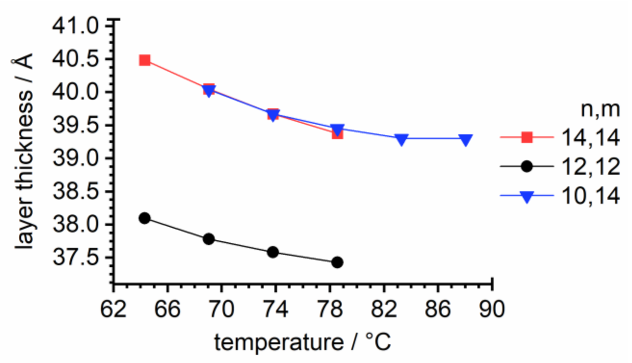

Figure 13. Determined layer distances *d*$_{001}$ of **3,4-C$_{14}$TyrC$_{10}$Cl**, **3,4-C$_{12}$TyrC$_{12}$Cl** and **3,4-C$_{14}$TyrC$_{14}$Cl** as a function of temperature.

Next the members of series **4-C$_{14}$TyrC$_{14}$X** and **3,4-C$_{14}$TyrC$_{14}$X** with different counterions were examined by XRD experiments (Figure 14, Table , Figure S16 – S18). In a similar fashion as observed for the chloride series **4-C$_m$TyrC$_n$Cl** and **3,4-C$_m$TyrC$_n$Cl** one distinct reflection assigned as (001) could be observed in the SAXS diffractograms of non-oriented samples together with a broad halo around 4.43 – 4.88 Å in the WAXS. Additionally, in all cases except the decomposing iodide **4-C$_{14}$TyrC$_{14}$I**, decreasing layer thickness (*d*$_{001}$) with increasing temperature could be observed in temperature-dependent SAXS experiments, confirming the predicted SmA$_d$ phases. The data in Table 4 indicated that the anion has a large impact on the layer thickness. For both series **4-C$_{14}$TyrC$_{14}$X** and **3,4-C$_{14}$TyrC$_{14}$X** (X = I, NO$_3$, BF$_4$, PF$_6$) the layer thickness decreased with increasing size of the anion. Presumably, larger anions such as hexafluorophosphate allow better space filling and thus tighter packing as compared to smaller anions such as iodide in agreement with previous work by Wang on *N*-phenylpyridinium ILCs.[74] It should be noted however, that the corresponding guanidinium chlorides **4-C$_{14}$TyrC$_{14}$Cl**, **3,4-C$_{14}$TyrC$_{14}$Cl** displayed much smaller *d* values as compared to **4-C$_{14}$TyrC$_{14}$PF$_6$**, **3,4-C$_{14}$TyrC$_{14}$PF$_6$**. This might be due to stronger hydrogen bonding between the chloride anion with the guanidinium N-H unit as compared to the other studied anions.[62,64] In contrast, Neidhardt did not observe any clear trend of the layer thickness in the series

C$_{14}$TyrC$_{14}$X upon change of the anion, but a change of the mesophase geometry from SmA (X = Cl, Br, I, OTf, BF$_4$) to Col$_h$ (X = PF$_6$).[52]

Table 4. X-ray diffraction data of the guanidinium salts **4-C$_{14}$TyrC$_{14}$X** and **3,4-C$_{14}$TyrC$_{14}$X** (SAXS). The measurements were performed during cooling from the isotropic liquid phase. The halo was determined from WAXS.

Ar	X	mesophase	*T* / °C	*d* spacing / Å	Miller indices
4	Cl	SmA$_d$	98	37.8	(001)
				4.60	halo
	I	SmA$_d$	95	44.0	(001)
				–	halo
	NO$_3$	SmA$_d$	76	42.5	(001)
				4.49	halo
	BF$_4$	SmA$_d$	61	41.5	(001)
				4.75	halo
	PF$_6$	SmA$_d$	70	39.8	(001)
				4.88	halo
3,4	Cl	SmA$_d$	74	39.7	(001)
				4.52	halo
	I	SmA$_d$	70	44.8 (WAXS)	(001)
				4.60	halo
	NO$_3$	SmA$_d$	61	44.3	(001)
				4.43	halo
	BF$_4$	SmA$_d$	80	43.3 (WAXS)	(001)
				4.82	halo
	PF$_6$	SmA$_d$	90	42.1	(001)
				4.63	halo

Although fiber extrusion of tyrosine-3,4,5-trisalkoxybenzoates **3,4,5-C$_m$TyrC$_n$Cl** did not provide oriented samples, the SAXS diffractogram of ILC **3,4,5-C$_{12}$TyrC$_{12}$Cl** showed three distinct reflections with a 2θ ratio of $1 : 1/\sqrt{3} : 1/2$, which were assigned as (10), (11) and (20) reflections (Figure 14). The WAXS diffractogram showed a broad halo around 4.47 Å. Thus, a Col$_h$ phase with *P6mm* symmetry and a lattice parameter of 43.8 Å (number of molecules per disc $Z = 4$) was assigned. Similar results were obtained for ILCs **3,4,5-C$_{10}$TyrC$_{14}$Cl** and **3,4,5-C$_{14}$TyrC$_{14}$Cl** respectively (Figure S19, Table).

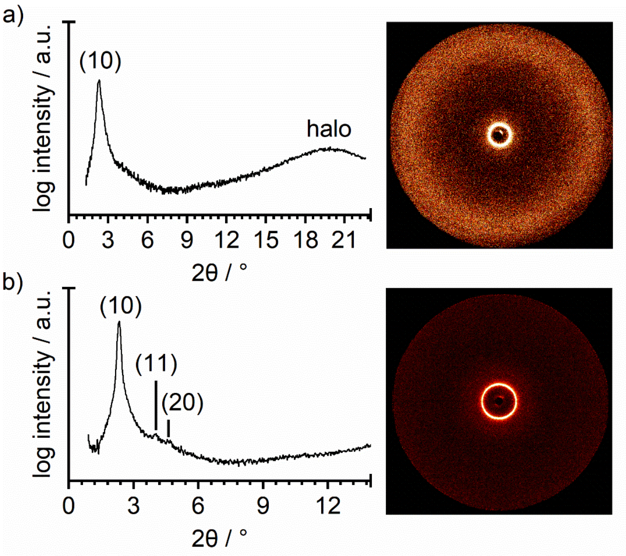

Figure 14. X-ray diffractograms (left) and 2D diffraction patterns (right) of **3,4,5-C$_{12}$TyrC$_{12}$Cl** at 79 °C in a) WAXS and b) SAXS.

Table 5. X-ray diffraction data of the guanidinium chlorides **3,4,5-C$_n$TyrC$_m$Cl** (SAXS). The measurements were performed during cooling from the isotropic liquid phase. The halo was determined from WAXS. Calculated values of *d* are in parentheses.

n	m	mesophase	*T* / °C	lattice *a* / Å	*d* spacing / Å	Miller indices	*Z*
10	14	Col$_h$ / *P6mm*	36	44.6	38.6 (–)	(10)	4
					4.46	halo	
12	12	Col$_h$ / *P6mm*	79	43.8	37.9 (–)	(10)	4
					22.0 (21.9)	(11)	
					19.1 (19.0)	(20)	
					4.47	halo	
14	14	Col$_h$ / *P6mm*	69	44.1	38.2 (–)	(10)	4
					4.42	halo	

As the ILCs **3,4,5-C$_m$TyrC$_n$Cl** do not resemble a discotic molecule but rather a wedge-shaped amphiphile, each disk in the columnar packing consists of 4 molecules in a pizza-slice arrangement with a charged core and a lipophilic outer shell (Figure 15). Such micellar-like structure of the columnar mesophase is in agreement with the packing pattern proposed by Neidhardt for the DOPA-derived ILCs **C$_m$DOPAC$_n$Cl**[25] as well as other wedge-shaped ILCs.[75–78] Differences in the phase behavior as well as in transition temperatures (in some cases ±42 – 51 K) of the chlorides **3,4,5-C$_m$TyrC$_n$Cl** and the compounds **C$_m$DOPAC$_n$Cl** can be attributed to the packing behavior and the number of molecules per disk (Z = 5 and 6).[25] In this context, a larger number of anion-cation pairs could lead to denser interdigitation and thus to denser packings within column. As already observed for the SmA mesophases of series **3,4-C$_m$TyrC$_n$Cl** the chain length of the ether side chains has the major influence on the lattice parameter. This is most obvious upon comparison of **3,4,5-C$_{14}$TyrC$_{10}$Cl** and **3,4,5-C$_{14}$TyrC$_{14}$Cl** possessing almost the same lattice parameter a = 44.6 Å and 44.1 Å respectively.

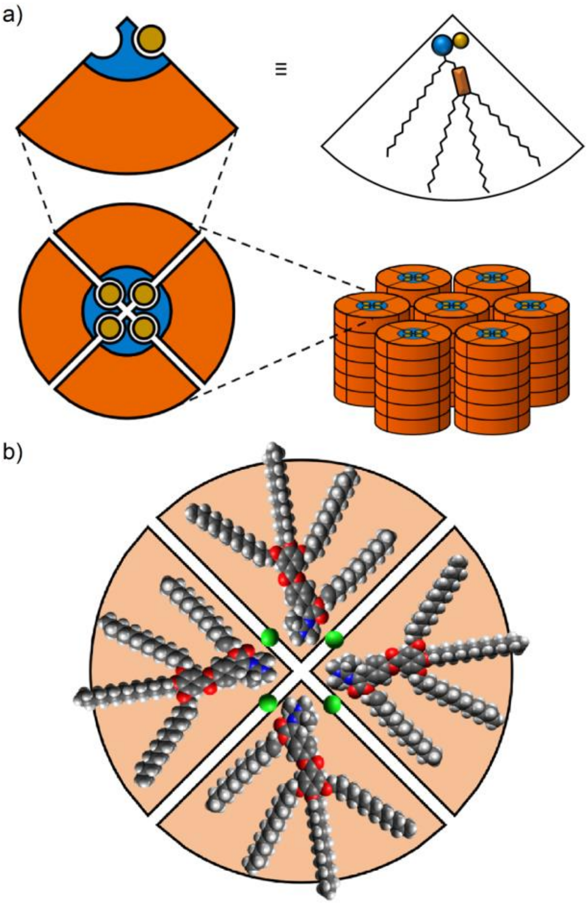

Figure 15. a) Proposed packing model with schematic representations of **3,4,5-C$_{14}$TyrC$_{14}$Cl** in pizza slice-like form (top) considering Neidhardts previous work,[25,32,59] after formation of a micellar disk (bottom left; Z = 4) and inverse columnar aggregates (bottom right): cationic head group (blue); chloride anion (yellow); periphery with aromatic system (orange) and chains. b) Four units of **3,4,5-C$_{14}$TyrC$_{14}$Cl** in an inverse micellar disk, visualised in a space-filling model; C (gray); H (white); O (red); N (blue); Cl (green).

Next the members of series **3,4,5-C$_{14}$TyrC$_{14}$X** with different counterions were examined by XRD experiments (Figure 16, Table , Figure S20). In a similar fashion as observed for the chloride series **3,4,5-C$_n$TyrC$_m$Cl** three distinct reflections assigned as (10), (11) and (20) were detected in the SAXS diffractograms of non-oriented samples together with a broad halo around 4.34 – 4.47 Å in the WAXS, which were assigned as Col$_h$ phase with *p6mm* symmetry (Z = 4). Fortunately, partially oriented SAXS patterns could by obtained for **3,4,5-C$_{14}$TyrC$_{14}$PF$_6$** and **3,4,5-C$_{14}$TyrC$_{14}$BF$_4$** respectively (Figure 17), which revealed that the (10) reflex consists of a hexagon with azimuthal angles of 60°, which strongly supports the Col$_h$ phase.[79,80]

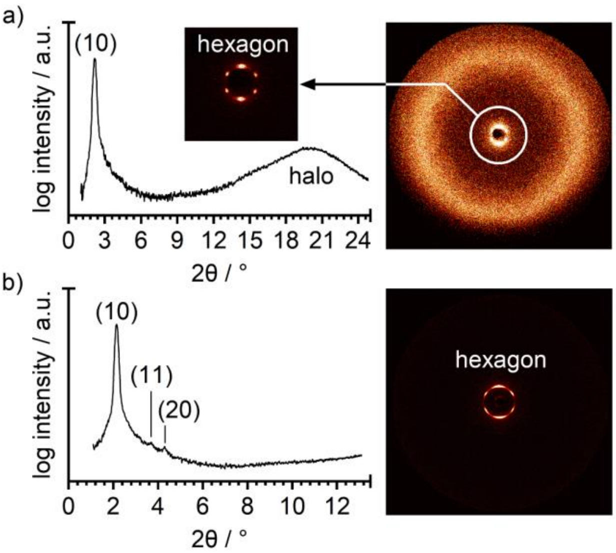

Figure 16. X-ray diffractograms (left) and 2D diffraction patterns (right) of a) **3,4,5-C$_{14}$TyrC$_{14}$PF$_6$** at 55 °C in WAXS and b) **3,4,5-C$_{14}$TyrC$_{14}$BF$_4$** at 55 °C in SAXS.

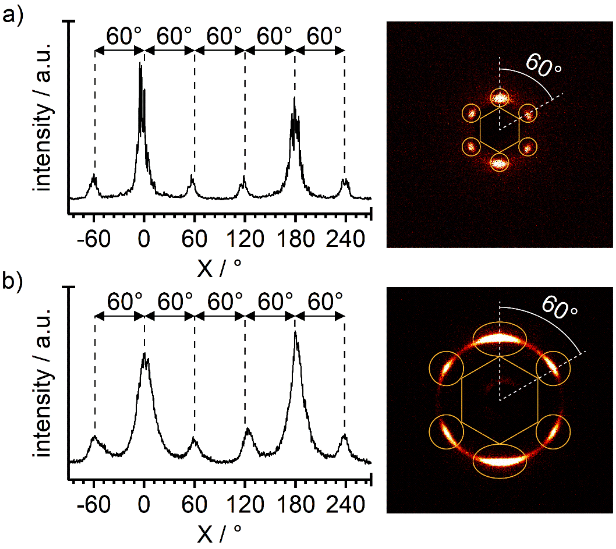

Figure 17. Azimuthal intensity profiles of the innermost hexagon (left) and corresponding 2D diffraction patterns (right; magnified) of the salts a) **3,4,5-C$_{14}$TyrC$_{14}$PF$_6$** in the WAXS and b) **3,4,5-C$_{14}$TyrC$_{14}$BF$_4$** in SAXS at 55 °C, respectively.

Table 6. X-ray diffraction data of the guanidinium salts **3,4,5-C$_{14}$TyrC$_{14}$X** (SAXS). The measurements were performed during cooling from the isotropic liquid phase. The halo was determined from WAXS. Calculated values of *d* are in parentheses.

X	mesophase	*T* / °C	lattice *a* / Å	*d* spacing / Å	Miller indices	*Z*
Cl	Col$_h$ / *P6mm*	69	44.1	38.2 (–)	(10)	4

					halo	
Br	$\mathrm{Col_h}$ / *P6mm*	55	46.2	40.0 (–)	(10)	4
				4.47	halo	
NO_3	$\mathrm{Col_h}$ / *P6mm*	55	46.7	40.4 (–)	(10)	4
				23.7 (23.3)	(11)	
				20.4 (20.2)	(20)	
				4.37	halo	
SCN	$\mathrm{Col_h}$ / *P6mm*	41	47.9	41.5 (–)	(10)	4
				24.0 (24.0)	(11)	
				20.8 (20.8)	(20)	
				4.34	halo	
I	$\mathrm{Col_h}$ / *P6mm*	55	46.2	40.0 (–)	(10)	4
				4.42	halo	
BF_4	$\mathrm{Col_h}$ / *P6mm*	55	47.5	41.2 (–)	(10)	4
				24.2 (23.8)	(11)	
				20.6 (20.6)	(20)	
				4.39	halo	
PF_6	$\mathrm{Col_h}$ / *P6mm*	55	48.1	41.6 (–)	(10)	4
				21.0 (20.8)	(20)	
				4.47	halo	

Comparison of the XRD data of **3,4,5-C_{14}TyrC_{14}X** in Table 6 revealed that the counterion size has a larger impact on the lattice parameters *a* as compared to the ether/ester side chain lengths. The *a* values increase with increasing size of the counterion, except for X = SCN, I. For example, both ILCs with Br and I counterion have similar lattice parameters ($a = 46.2$ and 46.2 Å) as well as ILCs with BF_4 and SCN ($a = 47.5$ and 47.9 Å) despite the different size of the counterions. These exemptions from the overall trend might be rationalized by the rod-like rather than spherical structure of SCN anion and the higher polarizability of iodide as compared to bromide resulting in tighter packing. The increasing *a*-values of **3,4,5-C_{14}TyrC_{14}X** with increasing counterion size and thus the decreased packing density can be correlated with the observed decrease of the mesophase stability (i.e. decreasing clearing temperatures) shown in Figure 8.[81] It should be noted that the number of molecules per disk *Z* does not change with the counterion. Also, no counterion-dependent change of the mesophase type was observed as reported for DOPA ILCs.[59] Thus, it seems that the pizza-slice arrangement of the tyrosine-3,4,5-alkoxybenzoate ILCs can accommodate counterions of various size without any problems.

Because the purpose of the featured guanidinium chlorides **Ar(C$_m$)TyrC$_n$Cl** was to be examined for biological activity, it could be beneficial to investigate the compounds for lyotropic liquid crystalline properties, i.e. mesomorphic behaviour in a suitable medium or solvent. Since the investigation of lyotropic properties is very time and resource consuming, only the chloride **3,4,5-C$_{10}$TyrC$_{14}$Cl** was initially investigated as part of these studies. First, the sample was examined in form of a contact preparation under a POM. Therefore, the sample was melted into the isotropic state, cooled to 40 °C and wetted with formamide. Water was excluded as a solvent because the guanidinium salts were insoluble in water. Furthermore, DMSO was also excluded because no textures could be observed. The dissolution process created a concentration gradient from the pure solvent to the pure compound, where textures formed depending on the local concentration (Figure 18a). Without XRD measurements, the exact mesophase geometries could not be determined, but the textures provided indications of possible cubic (I$_1$), hexagonal (H$_1$) (Figure 18a) as well as lamellar (L$_\alpha$) pashes (Figure 18a and b).[82–87]

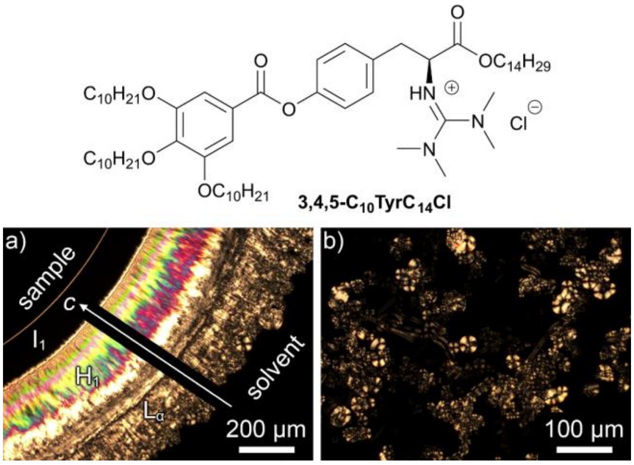

Figure 18. POM images of **3,4,5-C$_{10}$TyrC$_{14}$Cl** in a contact specimen with formamide (40 °C). Visible isotropic and homeotropic areas, respectively. a) rough mesophase assignment along the concentration gradient *c* (I$_1$: cubic phase, H$_1$: hexagonal phase, L$_\alpha$: lamellar phase), 100 × magnification; b) mosaic-like textures and Maltese crosses, 200 × magnification.

In addition, to confirm a lyotropic character due to surfactant-like behaviour, the surface tension of **3,4,5-C$_{10}$TyrC$_{14}$Cl** in formamide was investigated. With the use of a tensiometer, it was possible to obtain a sigmoidal curve in a concentration-dependent measurement, which is characteristic for typical surfactants (Figure 19).

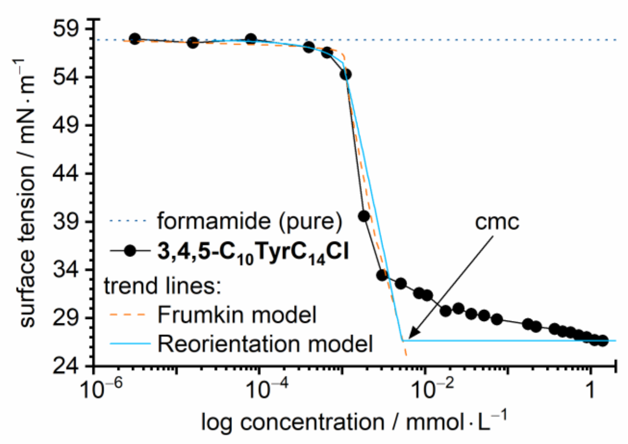

Figure 19. Determined surface tension of **3,4,5-C$_{10}$TyrC$_{14}$Cl** as a function of concentration (logarithmic scaling) of the sample in formamide (black line); trend lines according to the Frumkin (dashed orange line) and Reorientation model (light blue line); pure formamide (dotted dark blue line); cmc: critical micelle formation concentration.

By approximation using the Frumkin and Reorientation model,[88,89] the critical micelle formation concentration (cmc) could be determined to $\sim 5.7 \cdot 10^{-3}$ mmol · L^{-1}. The cmc value of a surfactant is essential for the formation of micelles and lyotropic mesophases. The determined value is lower than common surfactants in formamide, but is still within the typical range for surfactants.[90,91] The reason for this could be the relatively large cation, whereas the guanidinium head group should dissolve better in formamide due to its molecular structure.

Experimental dipole moment determination

We surmised that dipole interactions of the guanidinium salts not only contributed to their liquid crystalline self-assembly and phase behavior,[92–95] but might also affect their biological activities[96] and thus selected members were studied regarding their dipole moment. The dipole moments of the compounds **3,4,5-C$_{10}$TyrC$_{14}$Cl**, **BzTyrC$_{12}$Cl** and **3,4,5-C$_{10}$TyrC$_{12}$Cl** were experimentally determined by dielectric measurements of the compounds in toluene solution. The dipole moment of the molecules in solution was experimentally estimated according to the Guggenheim-Smith approach[97]

$$\mu^2 = \frac{27kTM}{4\pi N_a \rho_0 (\varepsilon_s + 2)^2} \left[\frac{\Delta\varepsilon}{w} - \frac{n^2 - n_s^2}{w}\right]. \quad (1)$$

Here, k is the Boltzmann constant, ρ_0 is the density of the solvent, N_a is the Avogadro number, $\Delta\varepsilon$ is the dielectric increment equals to the difference between the dielectric permittivity of the solution ε' and the solvent ε_s where w is the concentration of the solution. n and n_s represent the refraction indices of the solution and the solvent. The value of dipole moment was estimated by fitting a linear regression to the data in the plot $\Delta\varepsilon$ versus concentration (Figure 20). From the slope the dipole moment was obtained by equation (1). Here the difference in the square of the refractive indices is three orders of magnitudes smaller than $\Delta\varepsilon$[98] and this term is therefore neglected in the calculation of the dipole moment μ. Moreover, the fit was forced to go to the point of origin (see Figure 20). This means the data should hit the value of toluene at $w \rightarrow 0$. The calculated dipole moments along with the dielectric increments are presented in the Table 7. It must be noted that for these compounds, the ionic interactions dominate and hence a narrow range of low concentrations were chosen to minimize this effect. This effect also explains the higher scatter of the data compared to other investigations.[99]

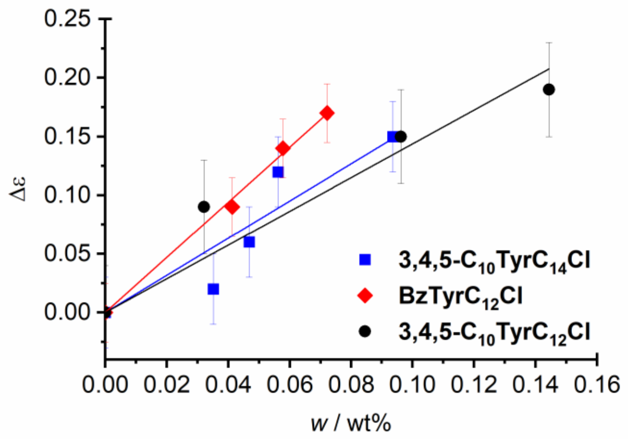

Figure 20. Plot of the dielectric increment $\Delta\varepsilon$ as a function of weight (wt%) for the compounds **3,4,5-C$_{10}$TyrC$_{14}$Cl**, **BzTyrC$_{12}$Cl** and **3,4,5-C$_{10}$TyrC$_{12}$Cl**.

Table 7 indicates that the dipole moments of all three compounds lie in the range of 1 – 1.2 D. It should be noted that the only difference in the structure **3,4,5-C$_{10}$TyrC$_{14}$Cl** and **3,4,5-C$_{10}$TyrC$_{12}$Cl** is the length of the alkyl chain. As the alkyl portion gives no contribution to the dipole moment both compounds carry in the frame of the of the experimental error the same dipole moment. This is different for **BzTyrC$_{12}$Cl**. Here in comparison to both other compounds some oxygen containing groups are missing which might contribute to the overall dipole moment. Therefore, **BzTyrC$_{12}$Cl** has the lowest dipole moment. Still, the compounds **BzTyrC$_{12}$Cl** and **3,4,5-C$_{10}$TyrC$_{12}$Cl** have a comparable dipole moment in the respective error region. Therefore, the question whether the dipole moment has an influence on the mesophase behavior cannot be answered conclusively, even though it seems that it is not the case.

Table 7. Determined dipole moments of the compounds **3,4,5-C$_{10}$TyrC$_{14}$Cl**, **BzTyrC$_{12}$Cl** and **3,4,5-C$_{10}$TyrC$_{12}$Cl**.

sample	$M / g \cdot mol^{-1}$	$\Delta\varepsilon$	dipole moment μ / D
3,4,5-C$_{10}$TyrC$_{14}$Cl	1085.1	1.58 ± 0.2	1.2 ± 0.07
BzTyrC$_{12}$Cl	588.2	2.35 ± 0.05	1.0 ± 0.02
3,4,5-C$_{10}$TyrC$_{12}$Cl	1057	1.44 ± 0.16	1.07 ± 0.07

Biological properties of tyrosine-derived ILCs

In an initial biological screening, tyrosine-derived ILCs **4-C$_m$TyrC$_n$Cl**, **3,4-C$_m$TyrC$_n$Cl**, **3,4,5-C$_m$TyrC$_n$Cl**, non-mesomorphic ILs **BzTyrC$_n$Cl**, **3,5-C$_m$TyrC$_n$Cl** and the crown ether derivatives **CrTyrC$_n$Cl** were examined. Spontaneous toxicity (24 h incubation time) was evaluated by the *CellTiter-Glo*® test,[100,101] longer-term cytotoxicity (72 h incubation time) was investigated by the *AlamarBlue*™ assay.[102,103] The mouse fibroblast cell line L929 was used as indicator cell line employing concentrations of 100 µM for 72 h at 37 °C. Antimicrobial activity against Gram-positive bacteria *Staphylococcus aureus* (*S. aureus*) and Gram-negative bacteria *Escherichia coli* (*E. coli*) K12 as well as the deletion mutant *E. coli* ΔTolC, which misses the export channel protein TolC, were evaluated with the broth dilution method[104] employing a concentration of 100 µM for 24 h. All compounds were evaluated in the same formats at lower concentrations of 20 µM (for bacteria) and 10 µM concentration (for L929 cells). These data are visualized in heat maps in the ESI (chapter 9.3, Figure S25 and S26). Only those compounds were considered as biologically active, which reduced bacterial growth or cell viability to less than 50% (with respect to the solvent control) at the lower concentrations. The heat map revealed for all guanidinium chlorides except for the benzoates **BzTyrC$_n$Cl** a low inhibitory action against all bacteria at 100 µM (darker spots). The benzoates **BzTyrC$_n$Cl** showed the strongest inhibition against *S. aureus* and the weakest inhibition against *E. coli* K12. Therefore, *E. coli* K12 was excluded from the subsequent dose-response studies.

The cell viability at 100 µM was slightly affected by members of the **3,4-C$_m$TyrC$_n$Cl** and **3,4,5-C$_m$TyrC$_n$Cl** series and a few other derivatives such as **4-C$_{10}$TyrC$_{10}$Cl**, but the most active compounds were benzoates **BzTyrC$_n$Cl** (Figure S26, ESI chapter 9.3). The latter derivatives displayed low cell viabilities (< 10%) even at concentrations of 10 µM.

Based on these primary screening results, dose-response studies were performed with selected compounds for the antibiotic activity (optical density OD_{600}, Figure 21b) and for the cytotoxic effects (fluorescence, Figure 21a). IC_{50} values were calculated from these data and visualised in Figure 22 and summarized in Table S8 in the ESI (chapter 9.3).

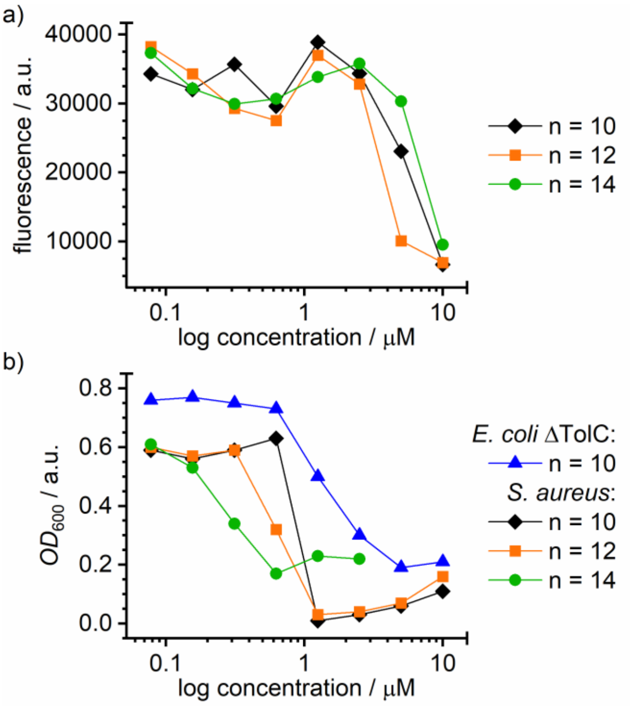

Figure 21. Graph of the inhibition by **BzTyrC$_n$Cl** against a) the cell viability (fluorescence) of L929 and b) the bacterial growth (optical density OD_{600}) of *E. coli* ΔTolC as well as *S. aureus* as a function of the concentration.

For comparison the data of crown ethers **CrTyrC$_n$Cl** were measured. Because of less comparable derivatives within this series, displaying heatmaps were not prepared. The results of the concentration series in a comparatively larger concentration range compared to **Ar(C$_m$)TyrC$_n$Cl** of the derivatives **CrTyrC$_{10}$Cl** and **CrTyrC$_{12}$Cl** can be found in Figure S27 in the ESI (chapter 9.3). Compound **CrTyrC$_{14}$Cl** was biological inactive. The results in Figure 22 (and Table S8, ESI chapter 9.3) revealed that both benzoates **BzTyrC$_n$Cl** as well as crown ethers **CrTyrC$_n$Cl** displayed a pronounced cytotoxicity with IC$_{50}$ values of 3.0 ± 1.1 up to 5.1 ± 1.6 μM irrespective of the ester chain lengths. Antimicrobial activities of crown ethers **CrTyrC$_n$Cl** were in a similar range with slightly lower IC$_{50}$ values against *S. aureus* (< 2.0 μM, 2.9 ± 0.2 μM) as compared to *E. coli* ΔTolC (3.8 ± 0.2 μM, 4.8 ± 1.1 μM). In contrast, IC$_{50}$ values of benzoates **BzTyrC$_n$Cl** were approximately one order of magnitude lower (0.25 – 0.9 μM for *S. aureus*, 1.3 ± 0.2 μM for *E. coli* ΔTolC) as compared to the cytotoxicity IC$_{50}$ values.

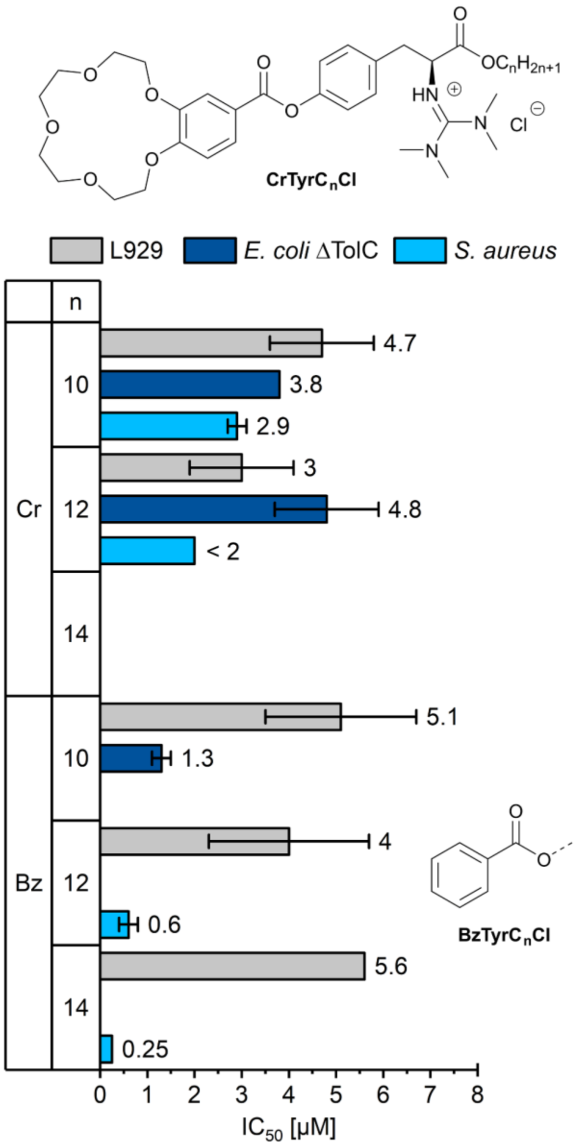

Figure 22. IC$_{50}$ values of guanidinium chlorides **CrTyrC$_n$Cl** (Cr) and **BzTyrC$_n$Cl** (Bz) versus cell line L929 and bacterial strains *E. coli* ΔTolC and *S. aureus* determined from graphical plotting (with error bars if mathematically determinable).

The different biological activities of the tyrosine benzoates might be rationalized as follows. According to Wang[105] amphiphilic compounds with long alkyl chains can be incorporated well into the outer membrane, however they do not fully penetrate the membrane and cannot pass into the interior of the cell. Thus, members of the series **4-C$_m$TyrC$_n$Cl**, **3,4-C$_m$TyrC$_n$Cl**, **3,5-C$_m$TyrC$_n$Cl** and **3,4,5-C$_m$TyrC$_n$Cl** are only weakly active. On the other hand, tyrosine benzoates **BzTyrC$_n$Cl** with only a single side chain seem to fully penetrate the membrane exerting their full anti-microbial potential, whereas the corresponding crown ethers **CrTyrC$_n$Cl** get stuck inside the membrane, facilitating ion transport through the membrane, but do not interact with the interior of the cell.[106] In comparison with the known amino acid ILCs **PheC$_n$Cl**, **C$_m$TyrC$_n$Cl** and **C$_m$DOPAC$_n$Cl**,[25] which were all cytotoxic irrespective of the amino acid, while only **PheC$_n$Cl** displayed weak antibiotic activity, tyrosine derivatives **Ar(C$_m$)TyrC$_n$Cl** with an extended aromatic core unit displayed only for those derivatives cytotoxic and antibiotic activity, if only the alkyl ester side chain is present. Ultimately, the thermotropic liquid crystalline properties do not seem to have a direct influence on the biological properties, at least in this case. Although the number of chains and the substitution pattern seem to play a role, there is no obvious correlation to the thermotropic mesophases formed. In this regard, the lyotropic liquid crystalline properties could provide additional insight and need to be further investigated in the future. With that said, in agreement with recent results by Garcia,[96] the antimicrobial activity of **BzTyrC$_n$Cl** could be somehow correlated with the higher dipole moment of **BzTyrC$_{12}$Cl** as compared to the inactive derivatives **3,4,5-C$_{10}$TyrC$_{12}$Cl** and **3,4,5-C$_{10}$TyrC$_{14}$Cl**. However, the compounds **BzTyrC$_{12}$Cl** and **3,4,5-C$_{10}$TyrC$_{12}$Cl** have quite different biological activities but with the error range a relatively comparable dipole moment. Therefore, the question whether the dipole moment contributes to the biological activity cannot be finally answered. Additional experimental investigations are necessary to tackle this problem. It should be noted that very recently Berthiot and Douce proposed that fluorescent ILCs might be valuable tools to gain insight into the link between molecular structure, mesophase type and biological properties.[107,108]

Conclusion

A series of tyrosine-derived guanidinium ILCs **Ar(C$_m$)TyrC$_n$X** was synthesized where the phenolic hydroxy group was esterified with benzoic acids carrying 0 – 3 alkoxy side chains or a [15]crown-5 unit respectively. Derivatives with only the C-terminal ester chain and no alkoxy chain at the benzoate were non-mesomorphic, while derivatives with 1 – 2 alkoxy chains at the benzoate displayed broad SmA$_d$ phases with clearing temperatures below 100 °C and phase widths up to 79 K. In particular, the mesomorphism of the ILCs with 3,4-dialkoxybenzoate unit turned out to be very robust, i.e. neither variation of chain lengths nor counterion changed the behaviour to large extent. In contrast, ILCs with 3,4,5-trialkoxybenzoate unit displayed broad $\mathrm{Col_h}$ phases with clearing temperatures ≤ 100 °C and phase widths up to 101 K. The phase stability was affected to some extent by the size matching of the side chains, i.e. derivatives **3,4,5-$\mathbf{C_{10}}$Tyr$\mathbf{C_{10}}$Cl**, **3,4,5-$\mathbf{C_{12}}$Tyr$\mathbf{C_{10}}$Cl**, **3,4,5-$\mathbf{C_{10}}$Tyr$\mathbf{C_{12}}$Cl**, **3,4,5-$\mathbf{C_{12}}$Tyr$\mathbf{C_{14}}$Cl** with short chains and/or chains of unequal lengths did not show any liquid crystalline behaviour. On the other hand, most counterions X (X = Cl, Br, I, PF_6, BF_4, NO_3) formed stable mesophases, whereas SCN significantly reduced the phase widths and stability and OTf completely suppressed mesophase formation.

In comparison with previously described tyrosine and DOPA ILCs[25] the presence of an additional benzoate unit in **Ar($\mathbf{C_m}$)Tyr$\mathbf{C_n}$X** shifted the mesophases to lower temperatures and required at least two side chains for stable mesomorphism. In agreement with these structure-property relationships crown ether derivatives **CrTyr$\mathbf{C_n}$Cl** were non-mesomorphic.[29]

Biological investigations of the newly synthesized tyrosine ILCs revealed that the bulk self-assembly was not correlated to cytotoxic or antimicrobial activity. Only the non-mesomorphic derivatives with benzoate (**BzTyr$\mathbf{C_n}$Cl**) or crown ether unit (**CrTyr$\mathbf{C_n}$Cl**) displayed pronounced cytotoxicity against L929 mouse fibroblast cells and antimicrobial activity against Gram-negative bacteria *E. coli* ΔTolC and Gram-positive bacteria *S. aureus* with IC_{50} values up to 3 μM, 1.3 μM, and 0.25 μM respectively. It should be noted that the incorporation of the benzoate unit improved the selectivity in favor of the antibiotic properties. In particular, the benzoates **BzTyr$\mathbf{C_n}$Cl** showed a better selectivity $S = IC_{50,\mathit{S.aureus}} / IC_{50,\mathrm{L929}} \leq 22$ as compared to the crown ether benzoates **CrTyr$\mathbf{C_n}$Cl** ($S \leq 1.6$) and the previously reported phenylalanine ILCs **Phe$\mathbf{C_n}$Cl** ($S \sim 0.7$).[25] Therefore, **BzTyr$\mathbf{C_n}$Cl** and **CrTyr$\mathbf{C_n}$Cl** might be promising lead structures for future biological SAR studies and investigations of the solvent-dependent self-assembly relevant for the interaction with bacterial membranes. Although the bioactive compounds **CrTyr$\mathbf{C_n}$Cl** and **BzTyr$\mathbf{C_n}$Cl** showed no thermotropic ionic liquid crystalline behaviour, they are ionic liquids, which might possess lyotropic properties. From complementary dielectric measurements of selected derivatives, one might conclude that a higher dipole moment and less side chains are beneficial for biological activity, whereas a lower dipole moment and more side chains are beneficial for thermotropic LC self-assembly.

For the reported series of tyrosine benzoates thermotropic liquid crystalline properties do not seem to determine antibiotic properties, as only the non-mesomorphic benzoic acid derivatives **BzTyrC$_n$Cl** showed biological activity. It should be noted however, that biological systems are always multicomponent systems and thus lyotropic studies might provide insight into the relationship between self-assembly of these compounds and cell membrane interactions.

Ultimately, the number of chain lengths and the substitution pattern of the tyrosine benzoates appear to play an important role in their interaction with cell membranes. These key parameters determine whether the compounds interfere with the membrane from the outside, are incorporated into it, or even permeate it completely and can exert their full potential inside the cell. Whether and to what extent LC self-assembly affects these processes must be investigated and clarified in the future, possibly with the help of fluorescent probes.[107,108] Thus, future work is necessary to elucidate the solvent-dependent behaviour of these compounds and their role as antibiotics.

Acknowledgement

Generous financial support by the Deutsche Forschungsgemeinschaft (LA 907/17-2, LA 907/21-1, SCHO 470/26-1), the Alfred Kärcher Förderstiftung (Forschungsvorhaben 2017), the Ministerium für Wissenschaft, Forschung und Kunst des Landes Baden-Württemberg, the Bundesministerium für Bildung und Forschung (shared instrumentation grant 01 RI05177), the Carl-Schneider-Stiftung Aalen, and the Fonds der Chemischen Industrie are gratefully acknowledged. We would like to thank Cosima Stubenrauch, Frank Giesselmann and Thomas Sottmann from the Institute of Physical Chemistry (University of Stuttgart) for providing equipment (tensiometer, POM) and Natalie Preisig for supervising the tensiometer measurements.

Conflicts of interest

There are no conflicts to declare.

Author contributions

M.A.G. designed the experiments and wrote the draft version of the manuscript. M.A.G., L.T. and S.B.W. synthesized the tyrosine ILCs. M.A.G and S.E.H. performed the salt metathesis reactions. L.A.A. performed the cytotoxicity and antimicrobial studies. S.M.B., M.E., J.A.K., A.R.R., and F.S. performed the SAXS and WAXS experiments. M.A.K. performed dielectric spectroscopy studies. A.Z. wrote the manuscript, coordinated assembly of the data and checked all experimental data. P.H. contributed his expertise regarding physico-chemical characterization, in particular XRD. A.S. supervised the dielectric spectroscopy experiments and contributed his expertise regarding physico-chemical characterization. U.B. contributed her expertise regarding biological studies und supervised the biological studies. S.L. supervised the research and wrote the manuscript. All authors edited and approved the final version of the manuscript.

References

1 Y. Abu-Lebdeh, A. Abouimrane, P.-J. Alarco and M. Armand, *J. Power Sources*, 2006, **154**, 255–261.

2 R. Kawano, Md. K. Nazeeruddin, A. Sato, M. Grätzel and M. Watanabe, *Electrochem. Commun.*, 2007, **9**, 1134–1138.

3 H. Cao-Cen, J. Zhao, L. Qiu, D. Xu, Q. Li, X. Chen and F. Yan, *J. Mater. Chem.*, 2012, **22**, 12842–12850.

4 W. S. Chi, H. Jeon, S. J. Kim, D. J. Kim and J. H. Kim, *Macromol. Res.*, 2013, **21**, 315–320.

5 T. Kato, *Angew. Chem. Int. Ed.*, 2010, **49**, 7847–7848.

6 A. Abate, A. Petrozza, G. Cavallo, G. Lanzani, F. Matteucci, D. W. Bruce, N. Houbenov, P. Metrangolo and G. Resnati, *J. Mater. Chem. A*, 2013, **1**, 6572–6578.

7 S. Tan, C. Wang and Y. Wu, *J. Mater. Chem. A*, 2013, **1**, 1022–1025.

8 A. Beneduci, S. Cospito, M. La Deda, L. Veltri and G. Chidichimo, *Nat. Commun.*, 2014, **5**, 3105.

9 S. Cospito, A. Beneduci, L. Veltri, M. Salamonczyk and G. Chidichimo, *Phys. Chem. Chem. Phys.*, 2015, **17**, 17670–17678.

10 M. Henmi, K. Nakatsuji, T. Ichikawa, H. Tomioka, T. Sakamoto, M. Yoshio and T. Kato, *Adv. Mater.*, 2012, **24**, 2238–2241.

11 K. Salikolimi, A. A. Sudhakar and Y. Ishida, *Langmuir*, 2020, **36**, 11702–11731.

12 N. Kapernaum, A. Lange, M. Ebert, M. A. Grunwald, C. Haege, S. Marino, A. Zens, A. Taubert, F. Giesselmann and S. Laschat, *ChemPlusChem*, 2022, **87**, e202100397.

13 K. Goossens, K. Lava, C. W. Bielawski and K. Binnemans, *Chem. Rev.*, 2016, **116**, 4643–4807.

14 M. Mansueto and S. Laschat, *Handb. Liq. Cryst.*, 2014, **6**, 231–280.

15 K. V. Axenov and S. Laschat, *Materials*, 2011, **4**, 206–259.

16 L. Douce, J.-M. Suisse, D. Guillon and A. Taubert, *Liq. Cryst.*, 2011, **38**, 1653–1661.

17 S. Chen and S. H. Eichhorn, *Isr. J. Chem.*, 2012, **52**, 830–843.

18 V. Causin, G. Saielli, in *Green Solvents II Prop. Appl. Ion. Liq.* (Eds.: A. Mohammad, Inamuddin), Springer, Dordrecht, **2012**, pp. 79–118.

19 K. Takashi, Y. Masafumi, in *Electrochem. Asp. Ion. Liq. 2nd Ed.* (Ed.: O. Hiroyuki), John Wiley & Sons, Inc., Hoboken, New Jersey, **2011**, pp. 375–392.

20 M. E. Forman, M. C. Jennings, W. M. Wuest and K. P. C. Minbiole, *ChemMedChem*, 2016, **11**, 1401–1405.

21 J. Gravel and A. R. Schmitzer, *Org. Biomol. Chem.*, 2017, **15**, 1051–1071.

22 K. S. Egorova and V. P. Ananikov, *ChemSusChem*, 2014, **7**, 336–360.

23 W. Dobbs, B. Heinrich, C. Bourgogne, B. Donnio, E. Terazzi, M.-E. Bonnet, F. Stock, P. Erbacher, A.-L. Bolcato-Bellemin and L. Douce, *J. Am. Chem. Soc.*, 2009, **131**, 13338–13346.

24 R. T. W. Huang, K. C. Peng, H. N. Shih, G. H. Lin, T. F. Chang, S. J. Hsu, T. S. T. Hsu and I. J. B. Lin, *Soft Matter*, 2011, **7**, 8392–8400.

25 M. M. Neidhardt, K. Schmitt, A. Baro, C. Schneider, U. Bilitewski and S. Laschat, *Phys. Chem. Chem. Phys.*, 2018, **20**, 20371–20381.

26 S. Tsuzaki, S. Usui, H. Oishi, D. Yasushima, T. Fukuyasu, T. Oishi, T. Sato and N. Chida, *Org. Lett.*, 2015, **17**, 1704–1707.

27 S.-H. Park, X. Jin, J.-C. Kang, C. Jung, S.-S. Kim, S.-S. Kim, K.-Y. Lee and W.-H. Ham, *Org. Biomol. Chem.*, 2015, **13**, 4539–4550.

28 L. Raguž, C.-C. Peng, M. Kaiser, H. Görls and C. Beemelmanns, *Angew. Chem. Int. Ed.*, 2022, **61**, e202112616.

29 U. Bilitewski, J. A. V. Blodgett, A.-K. Duhme-Klair, S. Dallavalle, S. Laschat, A. Routledge, and R. Schobert, *Angew. Chem. Int. Ed.*, 2017, **56**, 14360–14382.

30 M. C. Jennings, B. A. Buttaro, K. P. C. Minbiole and W. M. Wuest, *ACS Infect. Dis.*, 2015, **1**, 304–309.

31 G. McDonnell and A. D. Russell, *Clin. Microbiol. Rev.*, 1999, **12**, 147–179.

32 K. Bader, M. M. Neidhardt, T. Wöhrle, R. Forschner, A. Baro, F. Giesselmann and S. Laschat, *Soft Matter*, 2017, **13**, 8379–8391.

33 M. Mansueto, W. Frey and S. Laschat, *Chem. Eur. J.*, 2013, **19**, 16058–16065.

34 J. Wang, T. L. Greaves, D. F. Kennedy, A. Weerawardena, G. Song, C. J. Drummond, *Aust. J. Chem.*, 2011, **64**, 180–189.

35 S. T. Reddy, K. P. Krovi and M. J. Swamy, *Cryst. Growth Des.*, 2014, **14**, 4944–4954.

36 R. O. Brito, E. F. Marques, P. Gomes, M. João Araújo and R. Pons, *J. Phys. Chem. B*, 2008, **112**, 14877–14887.

37 P. A. Korchak, E. V. Alopina, I. B. Pukinsky and E. A. Safonova, *Fluid Phase Equilibria*, 2020, **525**, 112789.

38 Z. Huang, J. Zhang, Y. Liu, A. Song and J. Hao, *J. Mol. Liq.*, 2020, **301**, 112399.

39 S. Fujiwara, H. Ohno and T. Ichikawa, *Mol. Syst. Des. Eng.*, 2018, **3**, 668–676.

40 S. Fujiwara, H. Ohno, M. Yoshio, T. Kato and T. Ichikawa, *Bull. Chem. Soc. Jpn.*, 2017, **91**, 1–5.

41 Z. Song, X. Xin, J. Shen, J. Jiao, C. Xia, S. Wang and Y. Yang, *Colloids Surf. Physicochem. Eng. Asp.*, 2017, **518**, 7–14.

42 K. Fujimura, T. Ichikawa, M. Yoshio, T. Kato and H. Ohno, *Chem. Asian J.*, 2016, **11**, 520–526.

43 X.-J. Yang, P. Zhang, W. Lv, T. Zhou, P. Li and M. Zhao, *J. Surfactants Deterg.*, 2019, **22**, 515–523.

44 T. Ichikawa, K. Fujimura, M. Yoshio, T. Kato and H. Ohno, *Chem. Commun.*, 2013, **49**, 11746–11748.

45 K. Srinivasa Rao, T. Singh, T. J. Trivedi and A. Kumar, *J. Phys. Chem. B*, 2011, **115**, 13847–13853.

46 S. Z. Mohammady, M. Pouzot and R. Mezzenga, *Biophys. J.*, 2009, **96**, 1537–1546.

47 I. M. Shimul, R. M. Moshikur, K. Minamihata, M. Moniruzzaman, N. Kamiya and M. Goto, *J. Mol. Liq.*, 2022, **349**, 118103.

48 P. Yao, S. Li, A. Lambert, Q. Cheng, Z. Yang and X. Zhu, *ACS Sustain. Chem. Eng.*, 2021, **9**, 4157–4166.

49 H. Vanda, Y. Dai, E. G. Wilson, R. Verpoorte and Y. H. Choi, *Comptes Rendus Chim.*, 2018, **21**, 628–638.

50 L. van ‘t Hag, H.-H. Shen, T.-W. Lin, S. L. Gras, C. J. Drummond and C. E. Conn, *Langmuir*, 2016, **32**, 12442–12452.

51 Y. Xie, H. Xing, Q. Yang, Z. Bao, B. Su and Q. Ren, *ACS Sustain. Chem. Eng.*, 2015, **3**, 3365–3372.

52 C. P. Roll, A. G. Martin, H. Görls, G. Leibeling, D. Guillon, B. Donnio and W. Weigand, *J. Mater. Chem.*, 2004, **14**, 1722–1730.

53 S. Sauer, S. Saliba, S. Tussetschläger, A. Baro, W. Frey, F. Giesselmann, S. Laschat and W. Kantlehner, *Liq. Cryst.*, 2009, **36**, 275–299.

54 M. Butschies, J. C. Haenle, S. Tussetschläger and S. Laschat, *Liq. Cryst.*, 2013, **40**, 52–71.

55 O. J. Curnow, M. T. Holmes, L. C. Ratten, K. J. Walst and R. Yunis, *RSC Adv.*, 2012, **2**, 10794–10797.

56 J. Litterscheidt, J. S. Bandar, M. Ebert, R. Forschner, K. Bader, T. H. Lambert, W. Frey, A. Bühlmeyer, M. Brändle, F. Schulz and S. Laschat, *Angew. Chem. Int. Ed.*, 2020, **59**, 10557–10565.

57 T. Noguchi, K. Kishikawa and S. Kohmoto, *Liq. Cryst.*, 2008, **35**, 1043–1050.

58 D. Ailincai, L. Marin, S. Shova and C. Tuchilus, *Comptes Rendus Chim.*, 2016, **19**, 556–565.

59 M. M. Neidhardt, M. Wolfrum, S. Beardsworth, Wöhrle, W. Frey, A. Baro, C. Stubenrauch, F. Giesselmann and S. Laschat, *Chem. Eur. J.*, 2016, **22**, 16494–16504.

60 M. E. Maloulibibout, L. Noussi, P. Lareginie, A. Samat and R. Guglielmetti, *Mol. Cryst. Liq. Cryst. Sci. Technol. Sect. Mol. Cryst. Liq. Cryst.*, 1994, **246**, 177–181.

61 R. Vallakati and J. A. May, *J. Am. Chem. Soc.*, 2012, **134**, 6936–6939.

62 M. Butschies, S. Sauer, E. Kessler, H.-U. Siehl, B. Claasen, P. Fischer, W. Frey and S. Laschat, *ChemPhysChem*, 2010, **11**, 3752–3765.

63 N. Trbojevic, J. C. Haenle, T. Wöhrle, J. Kirres and S. Laschat, *Liq. Cryst.*, 2016, **43**, 1135–1147.

64 J. C. Haenle, M. M. Neidhardt, S. Beardsworth, J. Kirres, A. Baro and S. Laschat, *Aust. J. Chem.*, 2014, **67**, 1088–1099.

65 J. N. Sarmousakis and M. J. D. Low, *J. Phys. Chem.*, 1956, **60**, 1139–1140.

66 Y. Marcus, *J. Chem. Soc. Faraday Trans.*, 1993, **89**, 713–718.

67 W. Grochala, *Phys. Chem. Chem. Phys.*, 2017, **19**, 30964–30983.

68 D. M. Agra-Kooijman, S. Kumar, in *Handb. Liq. Cryst.* (Eds.: J.W. Goodby, C. Tschierske, P. Raynes, H. Gleeson, T. Kato, P.J. Collings), Wiley-VCH, Weinheim, Germany, **2014**, pp. 301–336.

69 K. Bader, C. Müller, Y. Molard, A. Baro, P. Ehni, J. Knelles and S. Laschat, *RSC Adv.*, 2020, **10**, 23999–24016.

70 J. P. F. Lagerwall, F. Giesselmann and M. D. Radcliffe, *Phys. Rev. E*, 2002, **66**, 031703.

71 P. H. J. Kouwer and T. M. Swager, *J. Am. Chem. Soc.*, 2007, **129**, 14042–14052.

72 J. W. Goodby, in *Handb. Liq. Cryst.* (Eds.: J.W. Goodby, C. Tschierske, P. Raynes, H. Gleeson, T. Kato, P.J. Collings), Wiley-VCH Verlag GmbH & Co. KGaA, Weinheim, Germany, **2014**, pp. 43–68.

73 J. N. Israelachvili, D. J. Mitchell and B. W. Ninham, *J. Chem. Soc. Faraday Trans. 2 Mol. Chem. Phys.*, 1976, **72**, 1525–1568.

74 R.-T. Wang, G.-H. Lee and C. K. Lai, *CrystEngComm*, 2018, **20**, 2593–2607.

75 T. Ichikawa, T. Kato and H. Ohno, *Chem. Commun.*, 2019, **55**, 8205–8214.

76 R. Watanabe, T. Sakamoto, K. Yamazoe, J. Miyawaki, T. Kato and Y. Harada, *Angew. Chem. Int. Ed.*, 2020, **59**, 23461–23465.

77 Y. Ishii, N. Matubayasi, G. Watanabe, T. Kato and H. Washizu, *Sci. Adv.*, 2021, **7**, eabf0669.

78 V. Percec, C. M. Mitchell, W.-D. Cho, S. Uchida, M. Glodde, G. Ungar, X. Zeng, Y. Liu, V. S. K. Balagurusamy and P. A. Heiney, *J. Am. Chem. Soc.*, 2004, **126**, 6078–6094.

79 S. Laschat, A. Baro, N. Steinke, F. Giesselmann, C. Hägele, G. Scalia, R. Judele, E. Kapatsina, S. Sauer, A. Schreivogel and M. Tosoni, *Angew. Chem. Int. Ed.*, 2007, **46**, 4832–4887.

80 S. K. Prasad, D. S. S. Rao, S. Chandrasekhar and S. Kumar, *Mol. Cryst. Liq. Cryst.*, 2003, **396**, 121–139.

81 We would like to thank one of the referees for pointing this out.

82 Y. Huang and S. Gui, *RSC Adv.*, 2018, **8**, 6978–6987.

83 H. Li, L. Dang, S. Yang, J. Li and H. Wei, *Colloids Surf. Physicochem. Eng. Asp.*, 2016, **495**, 221–228.

84 A. Nesrullajev and Y. Altınay, *J. Mol. Liq.*, 2020, **300**, 112175.

85 C. Calahorro, J. Muñoz, M. Berjano, A. Guerrero and C. Gallegos, *J. Am. Oil Chem. Soc.*, 1992, **69**, 660–666.

86 T. Dabadie, A. Ayral, C. Guizard, L. Cot, C. Lurin, W. Nie and D. Rioult, *J. Sol-Gel Sci. Technol.*, 1995, **4**, 107–116.

87 Y. Iwashita and H. Tanaka, *Nat. Mater.*, 2006, **5**, 147–152.

88 A. Frumkin, *Z. Für Phys. Chem.*, 1925, **116**, 466–484.

89 V. B. Fainerman, A. V. Mys, E. V. Aksenenko, A. V. Makievski, J. T. Petkov, J. Yorke and R. Miller, *Colloids Surf. Physicochem. Eng. Asp.*, 2009, **334**, 22–27.

90 M. S. Akhter and S. M. Alawi, *Colloids Surf. Physicochem. Eng. Asp.*, 2000, **173**, 95–100.

91 J.-M. Lin, M. Nakagawa, K. Uchiyama and T. Hobo, *Chromatographia*, 1999, **50**, 739–744.

92 B. D. Rabideau, M. Soltani, R. A. Parker, B. Siu, E. A. Salter, A. Wierzbicki, K. N. West and J. H. Davis, *Phys. Chem. Chem. Phys.*, 2020, **22**, 12301–12311.

93 K. Wendler, S. Zahn, F. Dommert, R. Berger, C. Holm, B. Kirchner and L. Delle Site, *J. Chem. Theory Comput.*, 2011, **7**, 3040–3044.

94 T. Cherian, D. R. Nunes, T. G. Dane, J. Jacquemin, U. Vainio, T. T. Myllymäki, J. V. Timonen, N. Houbenov, M. Maréchal and P. Rannou, *Adv. Funct. Mater.*, 2019, **29**, 1905054.

95 M. A. Kolmangadi, G. J. Smales, L. ZhuoQing, A. Yildirim, E. Wuckert, S. Eutionnat, F. Demel, P. Huber, S. Laschat and A. Schönhals, *J. Phys. Chem. C*, 2022, **126**, 10995–11006.

96 G. M. Reddy, G. Sravya, G. Yuvaraja, A. Camilo, G. V. Zyryanov and J. R. Garcia, *Res. Chem. Intermed.*, 2018, **44**, 7491–7507.

97 J. W. Smith, *Electric dipole moments*, Butterworth, 1955.

98 S. Kovshik, M. Mikhailova, G. Polushina, E. Rjumtsev, A. Kovshik and A. Lezov, *J. Non-Cryst. Solids*, 2005, **351**, 2723–2727.

99 J. Knelles, C. Wanner, F. Schulz, M. Freund, M. A. Kolmangadi, A. Baro, P. Huber, A. Schönhals and S. Laschat, *Liq. Cryst.*, 2021, **48**, 1382–1391.

100 T. O. Baldwin, *Structure*, 1996, **4**, 223–228.

101 H. Fraga, D. Fernandes, J. Novotny, R. Fontes and J. C. G. Esteves da Silva, *ChemBioChem*, 2006, **7**, 929–935.

102 Bio-Rad, What is alamarBlue?, https://www.bio-rad-antibodies.com/alamarblue-cell-viability-assay-resazurin.html (accessed February 26, 2022).

103 N. Shenoy, M. Stenson, J. Lawson, J. Abeykoon, M. Patnaik, X. Wu and T. Witzig, *Lab. Invest.*, 2017, **97**, 494–497.

104 I. Wiegand, K. Hilpert and R. E. W. Hancock, *Nat. Protoc.*, 2008, **3**, 163–175.

105 D. Wang, C. Richter, A. Rühling, P. Drücker, D. Siegmund, N. Metzler-Nolte, F. Glorius and H.-J. Galla, *Chem. Eur. J.*, 2015, **21**, 15123–15126.

106 A. Mai-Prochnow, M. Clauson, J. Hong and A. B. Murphy, *Sci. Rep.*, 2016, **6**, 38610.

107 R. Berthiot, N. del Giudice and L. Douce, *Eur. J. Org. Chem.*, 2021, **2021**, 4099–4106.

108 N. del Giudice, M. L'Her, E. Scrafton, Y. Atoini, G. Gentile, B. Heinrich, R. Berthiot, A. Aliprandi and L. Douce, *Eur. J. Org. Chem.*, 2021, **2021**, 2091–2098.